

# SPIDER - VII. Revealing the stellar population content of massive early-type galaxies out to 8Re

F. La Barbera, I. Ferreras, R. R. de Carvalho, G. Bruzual, S. Charlot, A. Pasquali, E. Merlin

▶ **To cite this version:**

F. La Barbera, I. Ferreras, R. R. de Carvalho, G. Bruzual, S. Charlot, et al.. SPIDER - VII. Revealing the stellar population content of massive early-type galaxies out to 8Re. Monthly Notices of the Royal Astronomical Society, 2012, 426, pp.2300-2317. 10.1111/j.1365-2966.2012.21848.x . hal-03645725

**HAL Id: hal-03645725**
**https://hal.science/hal-03645725**

Submitted on 6 Jun 2022

**HAL** is a multi-disciplinary open access archive for the deposit and dissemination of scientific research documents, whether they are published or not. The documents may come from teaching and research institutions in France or abroad, or from public or private research centers.

L'archive ouverte pluridisciplinaire **HAL**, est destinée au dépôt et à la diffusion de documents scientifiques de niveau recherche, publiés ou non, émanant des établissements d'enseignement et de recherche français ou étrangers, des laboratoires publics ou privés.

Monthly Notices of the ROYAL ASTRONOMICAL SOCIETY

Mon. Not. R. Astron. Soc. **426,** 2300–2317 (2012) doi:10.1111/j.1365-2966.2012.21848.x

# SPIDER – VII. Revealing the stellar population content of massive early-type galaxies out to $8R_e$

F. La Barbera,[1⋆] I. Ferreras,[2] R. R. de Carvalho,[3] G. Bruzual,[4] S. Charlot,[5,6] A. Pasquali[7] and E. Merlin[8]

[1]*INAF – Osservatorio Astronomico di Capodimonte, Napoli, Italy*
[2]*MSSL, University College London, Holmbury St Mary, Dorking, Surrey RH5 6NT*
[3]*Instituto Nacional de Pesquisas Espaciais/MCT, S. J. dos Campos, Brazil*
[4]*Centro de Radioastronomía y Astrofísica, UNAM, Campus Morelia, México*
[5]*UPMC, UMR7095, Institut d'Astrophysique de Paris, F-75014 Paris, France*
[6]*CNRS, UMR7095, Institut d'Astrophysique de Paris, F-75014 Paris, France*
[7]*Astronomisches Rechen Institut, Zentrum für Astronomie der Universität Heidelberg, Mönchhofstr. 12–14, 69120 Heidelberg, Germany*
[8]*INAF – Osservatorio Astronomico di Padova, Padova, Italy*

Accepted 2012 August 1. Received 2012 July 6; in original form 2012 May 26

**ABSTRACT**

Radial trends of stellar populations in galaxies provide a valuable tool to understand the mechanisms of galaxy growth. In this paper, we present the first comprehensive analysis of optical–optical and optical–NIR colours, as a function of galaxy mass, out to the halo region ($8R_e$) of early-type galaxies (ETGs). We select a sample of 674 massive ETGs ($M_\star \gtrsim 3 \times 10^{10}\,M_\odot$) from the Sloan Digital Sky Survey (SDSS)-based SPIDER survey. By comparing with a large range of population synthesis models, we derive robust constraints on the radial trends in age and metallicity. Metallicity is unambiguously found to decrease outwards, with a measurable steepening of the slope in the outer regions ($R_e < R < 8R_e$). The gradients in stellar age are found to be more sensitive to the models used, but in general, the outer regions of ETGs feature older populations compared to the cores. This trend is strongest for the most massive galaxies in our sample ($M_\star \gtrsim 10^{11}\,M_\odot$). Furthermore, when segregating with respect to large-scale environment, the age gradient is more significant in ETGs residing in higher density regions. These results shed light on the processes leading from the formation of the central core to the growth of the stellar envelope of massive galaxies. The fact that the populations in the outer regions are older and more metal-poor than in the core suggests a process whereby the envelope of massive galaxies is made up of accreted small satellites (i.e. minor mergers) whose stars were born during the first stages of galaxy formation.

**Key words:** galaxies: elliptical and lenticular, cD – galaxies: evolution – galaxies: formation – galaxies: fundamental parameters – galaxies: groups: general – galaxies: stellar content.

## 1 INTRODUCTION

The link between chemical and dynamical evolution in early-type galaxies (ETGs) has been studied for quite a long time through systematic measurements of colour gradients, which may lead us to understanding how the variations in the age and metallicity of the underlying stellar populations (SP) evolve as star formation proceeds through the history of the system (de Vaucouleurs 1961; Davies et al. 1987; Peletier et al. 1990; Ferreras et al. 2005; La Barbera & de Carvalho 2009). The theoretical models suggest that metallicity and age gradients arise naturally from the processes leading to galaxy formation, like in the 'in situ' collapse of a proto-galactic gas cloud (Carlberg 1984). The first rendition of this formation scenario, also known as monolithic collapse (Eggen, Lynden-Bell & Sandage 1962; Larson 1974, 1975), predicted steep metallicity gradients, while a revised monolithic model for the formation of ETGs led to shallower metallicity gradients (e.g. Pipino, DÉrcole & Matteucci 2008; Pipino et al. 2010). Simulations (see e.g. Kobayashi 2004) indicate that galaxy mergers will weaken the metallicity gradient, and lead to significant levels of star formation in the galaxy centre. More recently, cosmological simulations have brought to our attention the importance of cold accretion, as a viable way to form galaxies 'in situ', resembling the monolithic formation scenario (e.g. Kereš et al. 2005). It is still a matter of debate whether the metallicity gradient we measure today is a product of an old SP – reflecting mainly the initial conditions when the system collapsed – or results from more recent star formation episodes. Therefore,

⋆E-mail: flabarber@gmail.com

© 2012 The Authors
Monthly Notices of the Royal Astronomical Society © 2012 RAS

Downloaded from https://academic.oup.com/mnras/article/426/3/2300/988992 by guest on 06 June 2022

systematic measurements of colour gradients are of crucial importance to distinguish among different formation models of early-type systems. A proper constraint on the gradients of the properties of the underlying SPs will help understand the mass assembly process in ETGs.

In the past, spectroscopic indices were used to measure metallicity in ETGs, revealing the existence of radial gradients ranging from $-0.1$ to $-0.3$ dex per decade (Carollo, Danziger & Buson 1993; Davies, Sadler & Peletier 1993; Mehlert et al. 2003). The number of ETGs for which the radial dependence of age and metallicity extends beyond one effective radius is small for today standards, albeit growing. This is due to the difficulty in obtaining spectroscopic measurements at surface brightness below the background sky level. However, the availability of multi-waveband samples for a vast number of sources remedy this situation, allowing us to estimate colour gradients up to several effective radii at low to moderate redshifts (Wu et al. 2005; Tal & van Dokkum 2011, hereafter TvD11), and open the possibility of studying radial gradients at $z > 1$ (Gargiulo, Saracco & Longhetti 2011; Guo et al. 2011). An important caveat is that colours have to be modelled by a SP synthesis code. This approach has been used in the past for small samples of ETGs (e.g. Peletier et al. 1990; Saglia et al. 2000), while in the recent years, the study of large galaxy samples has mostly focused on the optical regime (e.g. Roche, Bernardi & Hyde 2010; Tortora et al. 2010; González-Pérez, Castander & Kauffmann 2011), where one has to contend with the age–metallicity–extinction degeneracy (Worthey 1994). Silva & Elston (1994), and more recently Roediger et al. (2011), have found evidence for significant age gradients in ellipticals, while independent works (e.g. Hinkley & Im 2001; Mehlert et al. 2003) found negligible age gradients, showing that the interpretation of colour gradients is a difficult task.

Another aspect of studying colour gradients in ETGs is to understand how this quantity relates to other observables and relationships so that we can build up a consistent galaxy formation and evolution framework. For instance, although ETGs obey specific scaling relations (e.g. Fundamental Plane), they may well represent different families according to the way mass was assembled during their history and the characterization of how mergers may have established the mass assembly is of unquestionable interest (e.g. Greene et al. 2012). As a first approximation, we would expect mergers to significantly affect the well-known scaling relations involving central velocity dispersion and SP properties, unless mass is accreted at very large radii. Theoretical and observational work has shown that the presence of tidal debris in the outskirts of ETGs may provide an essential piece of evidence to distinguish among different assembly scenarios (e.g. Duc & Renaud 2011). So far, most of the SP work was carried out within the central regions and mainly restricted to the optical regime. Extending the analysis to the outer regions with a combination of optical and near-infrared data is a key factor to better comprehend how galaxies form and assemble their baryons.

In this paper we combine optical (Sloan Digital Sky Survey–Data Release 6, SDSS–DR6; Adelman-McCarthy et al. 2008) and near-infrared (UKIRT Infrared Deep Sky Survey–Data Release 4, UKIDSS-DR4; Lawrence et al. 2007) data to study colour gradients in a sample of 674 ETGs located in different environments. The data were analysed with a dedicated pipeline that uses the package 2DPHOT (La Barbera et al. 2008). The high-quality image of both optical and NIR surveys enabled us to determine reliable colour gradients out to eight effective radii, as shown below. All systematic effects were carefully taken into account, including background subtraction; stacking of the colour profiles and the effect of the tails of the point spread functions (PSFs) in the redder bands, all of which are crucial for an accurate measurement of the colours in the outer regions. The results presented here confirm previous findings about the metallicity gradients, and show that age gradients may not be as negligible as some papers have reported in the past.

The layout of the paper is as follows. In Section 2 we present our sample of ETGs. Section 3 deals with the methodology followed to determine the colour profiles, and discusses possible sources of systematics. In Section 4 we present the median-stacked colour profiles of ETGs, from $g - r$ through $g - K$, out to a maximum galactocentric distance of $8R_e$, for different galaxy mass bins. Section 5 describes the fitting of the observed profiles with theoretical models based on different, state-of-the-art, SP synthesis codes. In Section 6 we show the results of the SP fits, i.e. how age and metallicity are found to vary from the centre to the external regions of ETGs. We also discuss the contribution of internal reddening. Section 7 shows how the inferred age and metallicity profiles are affected by galaxy environment, while in Section 8 we summarize the main findings of this paper. Throughout the paper, we adopt a standard $\Lambda$cold dark matter cosmology with $H_0 = 75\,\mathrm{km\,s^{-1}\,Mpc^{-1}}$, $\Omega_\mathrm{m} = 0.3$ and $\Omega_\Lambda = 0.7$.

## 2 THE SAMPLE

The present study is based on a set of 674 ETGs, extracted from the Spheroid's Panchromatic Investigation in Different Environmental Regions (SPIDER) survey (La Barbera et al. 2010a, hereafter Paper I). This sample selects those galaxies with the best quality of the parameters that describe their surface brightness distributions. The SPIDER sample consists of 39 993 luminous ETGs, in the redshift range of 0.05 to 0.095, with $M_r < -20$, where $M_r$ is the k-corrected SDSS Petrosian magnitude in $r$ band. All galaxies have *griz* photometry and spectroscopy from SDSS-DR6, while 5080 ETGs also have photometry in the *YJHK* wavebands from the UKIDSS-Large Area Survey (see Paper I). In all wavebands, the structural parameters, i.e. the effective radius, $R_e$, mean surface brightness within that radius, $\langle\mu\rangle_e$, and Sérsic index, $n$, have been homogeneously measured using the software 2DPHOT (La Barbera et al. 2008), by fitting galaxy images with two-dimensional seeing-convolved Sérsic models. Total magnitudes are computed from $R_e$ and $\langle\mu\rangle_e$ in each filter. Stellar masses are derived by fitting synthetic SP models from Bruzual & Charlot (2003, hereafter BC03), with a variety of star formation histories and metallicities, to the optical+NIR photometry, using the software LEPHARE (Ilbert et al. 2006), assuming a Cardelli, Clayton & Mathis (1989) extinction law and Chabrier initial mass function (IMF; see Swindle et al. 2011, hereafter Paper V, for details on the estimate of $M_\star$).

To perform an accurate stacking of the surface brightness profiles (seeing de-convolved) as a function of galactocentric distance (see Section 3), we select ETGs according to the following criteria.

(i) We select only galaxies whose light distribution is well fitted by a Sérsic model, i.e. with $\chi^2 < 2$ in all wavebands, where $\chi^2$ is the rms of residuals between the galaxy image in a given band and the corresponding best-fitting two-dimensional Sérsic model. We also remove galaxies with large uncertainties (>0.5 dex) in $\log R_e$, leading to a sample of 4546 (out of 5080) ETGs. This sample is the same one used in La Barbera et al. (2010c, hereafter Paper IV), where the inner ($<1\,R_e$) colour gradients were analysed, along with their dependence on mass and SP properties (i.e. age, metallicity, and [$\alpha$/Fe]).

(ii) We select galaxies in a narrow redshift range, from 0.05 to 0.07, which corresponds to those with the best signal-to-noise ratio (S/N), minimizing the effect of k- and evolutionary corrections

Downloaded from https://academic.oup.com/mnras/article/426/3/2300/988992 by guest on 06 June 2022

varying within the sample and as a function of galactocentric distance. This results in 1255 ETGs.

(iii) Galaxies with stellar mass less than $M_\star = 3 \times 10^{10}\,M_\odot$ are removed, leading to 1043 ETGs. The reason for this selection is the following. At the upper redshift limit of $z = 0.095$, the magnitude limit of the SPIDER sample ($M_r \sim -20$; see above) corresponds approximately to the magnitude limit below which SDSS spectroscopy becomes incomplete (i.e. a Petrosian magnitude of $m_r \sim 17.8$). This makes the SPIDER sample incomplete at a stellar mass of $M_\star \sim 10^{10}\,M_\odot$ (corresponding to $M_r \sim -20$). The selection limit of $M_\star = 3 \times 10^{10}\,M_\odot$ ensures that the sample of ETGs used for the present analysis is 90 per cent complete with respect to stellar mass, this completeness level being estimated from the $M_\star$ versus $r$-band Petrosian magnitude plot (see e.g. section 3.2 of Paper IV).

(iv) Finally we remove galaxies with an axis ratio, $b/a \leq 0.65$. The reason for this selection is illustrated in Fig. 1, that compares the $r$-band median-stacked surface brightness profiles (solid red curves) of the 1043 ETGs at $0.05 \leq z \leq 0.07$ (see above) for three different bins of $b/a$ (from top to bottom) and $M_\star$ (from left to right). For a given bin of $M_\star$, the median profile corresponding to the highest $b/a$ is shown in all the panels as a dashed curve. At all masses, the profile does not change significantly (within a few per cent) for $b/a \gtrsim 0.65$, justifying our cut based on $b/a$. As argued by Hyde & Bernardi (2009), ETGs with $b/a \lesssim 0.6$ may indeed represent a different population of objects (e.g. rotationally supported systems).

Our final sample of high-quality data comprises 674 ETGs, and we split this sample in three bins of stellar mass, keeping the number of galaxies per bin fixed. Hereafter, we refer to galaxies in the three bins as low ($3.00 < M_\star[10^{10}\,M_\odot] < 5.29$), intermediate ($5.29 < M_\star[10^{10}\,M_\odot] < 9.42$) and high ($9.42 < M_\star[10^{10}\,M_\odot] < 70.71$) mass, respectively. In each bin of galaxy mass, we also split galaxies according to the environment where they reside. To this effect, we use the friends-of-friends (FoF) group catalogue, as described in Berlind et al. (2006). We use an updated catalogue based on SDSS-DR7 – rather than DR3, used for the original Berlind et al.

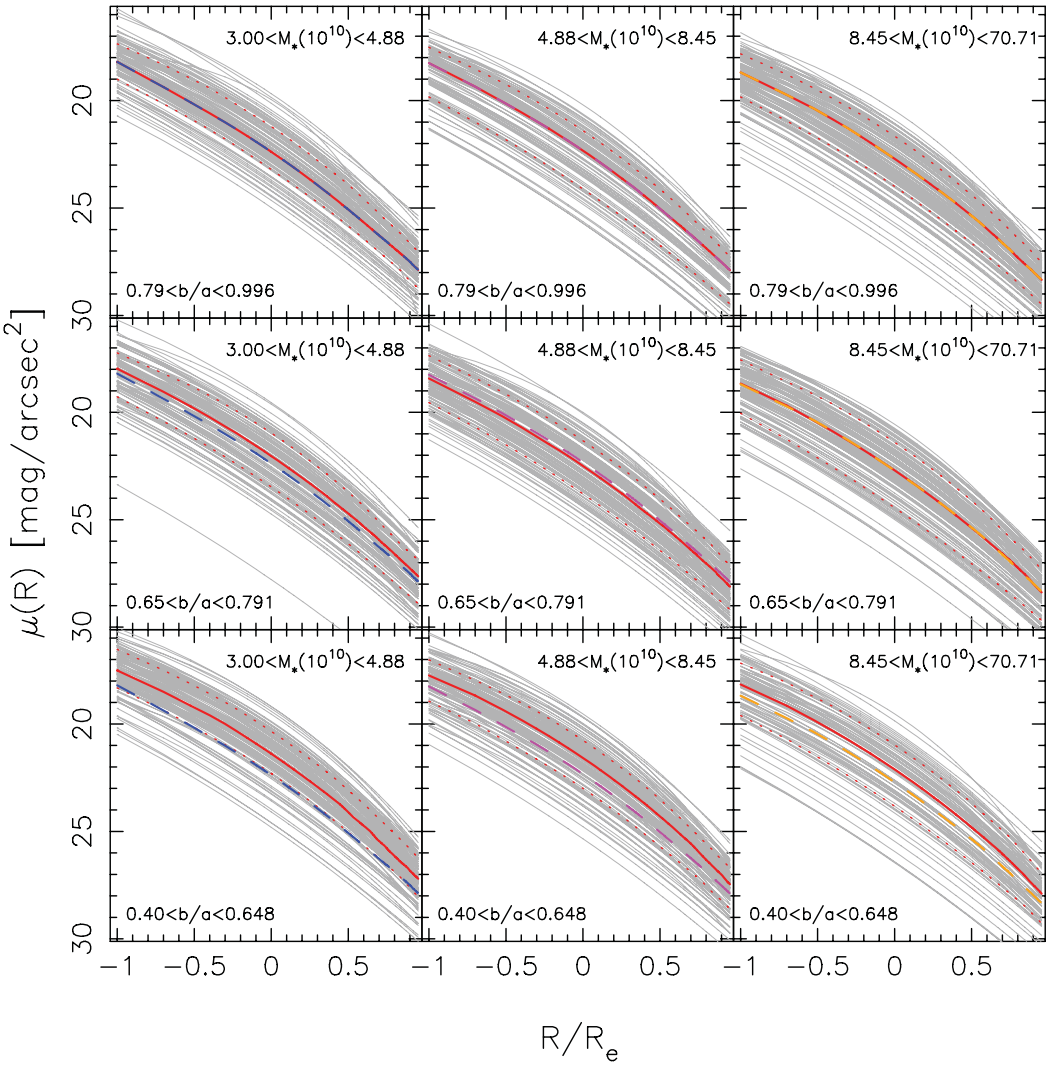



**Figure 1.** Comparison of the median surface brightness profiles of ETGs in different bins of stellar mass, $M_\star$ (increasing from left to right), and axis ratio, $b/a$ (decreasing from top to bottom). For each panel (i.e. a given bin of $M_\star$ and $b/a$), black curves plot the $r$-band surface brightness profiles of all galaxies in that bin. The profiles are shown as a function of the normalized galactocentric distance $R/R_e$, where $R_e$ is the $r$-band effective radius. For each panel, the solid red curve is obtained by median-stacking all the single profiles, with dotted curves marking the $\pm 1\sigma$ scatter around the median profiles. For each bin of $M_\star$, the median profile that corresponds to highest $b/a$ (top panel) is repeated in all panels (from top to bottom) as a coloured dashed curve (blue, magenta and orange for left, middle and right panels, respectively).

Downloaded from https://academic.oup.com/mnras/article/426/3/2300/988992 by guest on 06 June 2022

(2006) data set. The catalogue, which comprises 10 124 systems, is subject to a virial analysis (see Lopes et al. 2009, and references therein), resulting in a compilation of 8083 groups with well-measured properties (see La Barbera et al. 2010b, hereafter Paper III, for details). ETGs in the SPIDER sample are then classified as either (i) group galaxies, i.e. those having group membership according to the virial analysis (∼46 per cent), or (ii) field galaxies (∼33 per cent), i.e. objects located more than five virial radii away from any group initially detected by the FoF algorithm, or (iii) unclassified (∼21 per cent), i.e. objects in neither of the other two classes. Out of the selected sample of 674 ETGs analysed in the present work, 336 (205) objects are group (field) galaxies. The group galaxies reside in systems with average velocity dispersion (virial mass) of $\sim$240 km s$^{-1}$ ($\sim 8 \times 10^{13}$ M$_\odot$). These subsamples are used to investigate the dependence of SP profiles in ETGs on environment (Section 7).

## 3 DERIVATION OF COLOUR PROFILES

### 3.1 Methodology

For a given waveband $X$, with $X = grizYJHK$, the surface brightness profile of each ETG, $\mu_X(R)$, is modelled by the Sérsic law:

$$\mu_X(R) = \mu_{0,X} + 1.0857\, b_{n,X} \left(\frac{R}{R_{e,X}}\right)^{1/n_X}, \quad (1)$$

where $\mu_{0,X}$ is the central surface brightness of the Sérsic model in the passband $X$; $n_X$ is the corresponding Sérsic (shape) parameter; and $b_{n,X} \sim 2n_X - 1/3$ is a constant defined so that $R_{e,X}$ is the half-light radius of the model (Caon, Capaccioli & D'Onofrio 1993). The radius, $R$, is the circularized galactocentric distance. For each galaxy we construct the colour profile, in the form $g - X$ (with $X = rizYJHK$), by computing the difference of the corresponding Sérsic profiles:

$$g - X\,(R) = \mu_{0,g} - \mu_{0,X} + 1.0857 \left[ b_{n,g} \left(\frac{R}{R_{e,g}}\right)^{1/n_g} - b_{n,X} \left(\frac{R}{R_{e,X}}\right)^{1/n_X} \right]. \quad (2)$$

All the parameters, $\mu_{0,X}$, $R_{e,X}$ and $n_X$, are obtained by fitting the galaxy image in waveband $X$ with a PSF-convolved Sérsic model, as detailed in Paper I. For a given galaxy mass bin, a stacked colour profile is then computed. To this effect, for a given galaxy mass bin, the galactocentric radii of each individual colour profile are normalized by the corresponding $R_{e,r}$, and the median of all the so-normalized colour profiles is computed.

### 3.2 Systematics

At the very faint surface brightness levels we want to explore (i.e. $\gtrsim$25 mag arcsec$^{-2}$ in the $r$ band, at distances larger than a few effective radii; see Fig. 1), the colour profile of ETGs can be affected by several sources of systematics. We discuss here the role of such systematics, and how we take them into account in the analysis.

*Background subtraction.* As described in Paper I, structural parameters of ETGs are estimated by fitting galaxy images with a PSF-convolved Sérsic model plus a constant value representing the background. An error in the background estimate can bias the $R_{e,X}$ and $n_X$ parameters, changing the shape of the colour profiles (see equation 2). To quantify the relevance of this effect, we have repeated the Sérsic fitting in $g$ and $r$ bands, fixing the background to the value measured in the outermost regions of each postage stamp frame by applying the biweight statistics (Beers, Flynn & Gebhardt 1990). We found that the stacked $g - r$ colour profile does not change significantly when using a fixed-background fitting (with respect to the case where background is treated as a free fitting parameter), with a variation <0.02 mag arcsec$^{-2}$ at the largest radii probed ($R/R_e = 8$), i.e. smaller than the typical statistical error of the stacked profiles at these radii ($\gtrsim$0.03 mag arcsec$^{-2}$; see Tables 1–3). In this work, we use structural parameters, and hence colour profiles, derived by treating the background as a free fitting parameter (i.e. adopting the same procedure as in Paper I).

*Parametric versus non-parametric profiles.* Our stacked colour profiles are obtained by a parametric approach, using the best-fitting Sérsic models in different wavebands to compute the colour profiles. This approach is well justified by the fact that, on average, the light profiles of massive ellipticals are well described by a single Sérsic model out to roughly eight effective radii (Kormendy et al. 2009; TvD11). Moreover, the $\chi^2$ selection (see Section 2) allows us to exclude galaxies whose light profile is not reproduced by the Sérsic model. These objects are mostly early-spiral contaminants

**Table 1.** Median colours of low-mass ETGs at different galactocentric distances.

| $R/R_e$ | $g-r$ | $g-i$ | $g-z$ | $g-Y$ | $g-J$ | $g-H$ | $g-K$ |
|---|---|---|---|---|---|---|---|
| 0.1 | 0.871 ± 0.009 | 1.264 ± 0.011 | 1.588 ± 0.011 | 2.382 ± 0.015 | 2.882 ± 0.015 | 3.588 ± 0.016 | 3.957 ± 0.017 |
| 0.5 | 0.829 ± 0.005 | 1.201 ± 0.006 | 1.479 ± 0.008 | 2.245 ± 0.010 | 2.741 ± 0.013 | 3.389 ± 0.012 | 3.732 ± 0.014 |
| 1.0 | 0.805 ± 0.006 | 1.186 ± 0.007 | 1.450 ± 0.009 | 2.178 ± 0.012 | 2.665 ± 0.015 | 3.311 ± 0.014 | 3.649 ± 0.016 |
| 2.0 | 0.782 ± 0.008 | 1.166 ± 0.009 | 1.431 ± 0.012 | 2.130 ± 0.016 | 2.579 ± 0.026 | 3.242 ± 0.019 | 3.576 ± 0.026 |
| 4.0 | 0.740 ± 0.015 | 1.151 ± 0.017 | 1.431 ± 0.022 | 2.067 ± 0.029 | 2.427 ± 0.043 | 3.178 ± 0.031 | 3.475 ± 0.040 |
| 8.0 | 0.695 ± 0.028 | 1.157 ± 0.033 | 1.412 ± 0.040 | 1.964 ± 0.048 | 2.263 ± 0.072 | 3.091 ± 0.054 | 3.372 ± 0.062 |

**Table 2.** Median colours of intermediate-mass ETGs at different galactocentric distances.

| $R/R_e$ | $g-r$ | $g-i$ | $g-z$ | $g-Y$ | $g-J$ | $g-H$ | $g-K$ |
|---|---|---|---|---|---|---|---|
| 0.1 | 0.873 ± 0.008 | 1.284 ± 0.009 | 1.588 ± 0.009 | 2.413 ± 0.011 | 2.936 ± 0.012 | 3.615 ± 0.014 | 3.984 ± 0.014 |
| 0.5 | 0.838 ± 0.005 | 1.224 ± 0.007 | 1.500 ± 0.009 | 2.251 ± 0.011 | 2.758 ± 0.013 | 3.401 ± 0.014 | 3.750 ± 0.016 |
| 1.0 | 0.819 ± 0.006 | 1.192 ± 0.008 | 1.465 ± 0.010 | 2.174 ± 0.014 | 2.651 ± 0.019 | 3.305 ± 0.016 | 3.659 ± 0.018 |
| 2.0 | 0.792 ± 0.009 | 1.175 ± 0.012 | 1.437 ± 0.014 | 2.086 ± 0.019 | 2.539 ± 0.032 | 3.207 ± 0.027 | 3.546 ± 0.027 |
| 4.0 | 0.768 ± 0.019 | 1.173 ± 0.022 | 1.401 ± 0.024 | 2.006 ± 0.032 | 2.391 ± 0.053 | 3.099 ± 0.042 | 3.426 ± 0.043 |
| 8.0 | 0.732 ± 0.034 | 1.182 ± 0.039 | 1.383 ± 0.039 | 1.899 ± 0.050 | 2.206 ± 0.089 | 2.981 ± 0.063 | 3.285 ± 0.067 |

Downloaded from https://academic.oup.com/mnras/article/426/3/2300/988992 by guest on 06 June 2022

**Table 3.** Median colours of high-mass ETGs at different galactocentric distances.

| $R/R_e$ | $g-r$ | $g-i$ | $g-z$ | $g-Y$ | $g-J$ | $g-H$ | $g-K$ |
|---|---|---|---|---|---|---|---|
| 0.1 | $0.879 \pm 0.005$ | $1.286 \pm 0.006$ | $1.610 \pm 0.007$ | $2.434 \pm 0.010$ | $2.965 \pm 0.012$ | $3.639 \pm 0.013$ | $4.027 \pm 0.014$ |
| 0.5 | $0.844 \pm 0.005$ | $1.245 \pm 0.006$ | $1.529 \pm 0.008$ | $2.275 \pm 0.011$ | $2.792 \pm 0.014$ | $3.435 \pm 0.013$ | $3.789 \pm 0.015$ |
| 1.0 | $0.822 \pm 0.006$ | $1.225 \pm 0.007$ | $1.500 \pm 0.009$ | $2.200 \pm 0.014$ | $2.650 \pm 0.020$ | $3.355 \pm 0.017$ | $3.699 \pm 0.020$ |
| 2.0 | $0.801 \pm 0.010$ | $1.205 \pm 0.011$ | $1.473 \pm 0.015$ | $2.110 \pm 0.023$ | $2.492 \pm 0.034$ | $3.267 \pm 0.027$ | $3.604 \pm 0.029$ |
| 4.0 | $0.759 \pm 0.020$ | $1.193 \pm 0.022$ | $1.416 \pm 0.026$ | $2.009 \pm 0.041$ | $2.336 \pm 0.063$ | $3.145 \pm 0.045$ | $3.498 \pm 0.048$ |
| 8.0 | $0.703 \pm 0.035$ | $1.202 \pm 0.040$ | $1.373 \pm 0.046$ | $1.863 \pm 0.064$ | $2.099 \pm 0.099$ | $3.047 \pm 0.072$ | $3.375 \pm 0.073$ |

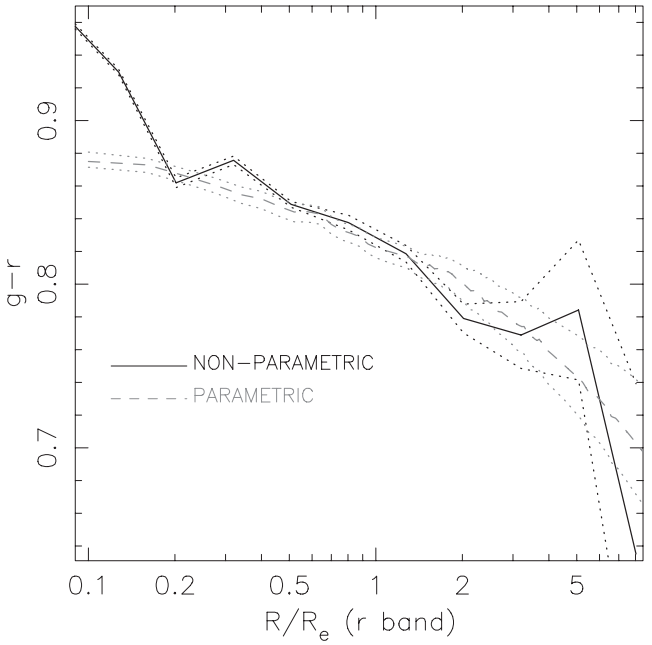



**Figure 2.** Median colour profiles of high-mass ETGs as obtained by the parametric (dashed curve) and non-parametric (solid curve) approaches (see text for details). Dotted grey (black) curves mark the $\pm 1\sigma$ error on the parametric (non-parametric) profile. The bump in the inner ($R/R_e < 0.2$) part of the non-parametric profile is due to the variation of the PSF between the $g$ and $r$ bands (the latter having a smaller full width at half-maximum, producing the red bump). The profiles are in good agreement within the scatter out to the largest radii probed in the present study ($\sim 8R_e$). Notice how the scatter in the non-parametric profile increases significantly at large galactocentric distances.

(see Paper I for details). In Appendix A we show the quality of our Sérsic fits by comparing the (stacked) best-fitting light profiles, derived on circular apertures, with those measured directly from the galaxy images, for all relevant wavebands and each mass bin. Parametric and non-parametric light profiles turn out to be fairly consistent, within uncertainties, supporting the robustness of our measurements out to large galactocentric distances. A further test of our parametric approach is illustrated in Fig. 2, comparing, as example, the stacked $g-r$ profiles obtained by the parametric and non-parametric approaches for high-mass ETGs. Our choice of $g-r$ for the comparison, rather than other colour profiles, is justified by the fact that this colour is less sensitive to the effect from the wings of the PSF (see below). Also, because of the shorter wavelength baseline with respect to other colours, $g-r$ provides a more critical test. For each galaxy, we measured the surface brightness profiles in the $g$ and $r$ bands directly from the images over the same concentric ellipses in both bands; all ellipses having the same axis ratio from the $r$-band Sérsic fit and circularized radii equally spaced by 0.5 pixel (i.e. $\sim 0.03\,R_e$ for high-mass ETGs). For each galaxy, we then rescaled the radii of the ellipses by a factor of $1/R_e$, where $R_{e,r}$ is the $r$-band effective radius of the given galaxy. The rescaled profiles were median-combined in both $g$ and $r$ bands to generate the non-parametric $g-r$ stacked colour profile. The stacked non-parametric profile was then averaged over radial bins logarithmically spaced by 0.15 dex, the profile uncertainty in each bin being computed from the standard deviation of colour values in the bin. Fig. 2 shows that parametric and non-parametric profiles differ significantly only in the inner part, at $R/R_e < 0.2$, as expected, since the non-parametric profile is not corrected for seeing effects, while they agree quite well out to a galactocentric distance of $\sim 3$–$4\,R_e$. We decide to continue our study using the parametric approach (i.e. Sérsic fitting) as the corresponding uncertainties in the surface brightness photometry are significantly smaller at large $R/R_e$, with respect to the case where a non-parametric approach is adopted – a crucial aspect for the present study.

*PSF red haloes.* The shape of the PSF at large radii can alter the colour profile of a galaxy. As regards SDSS data, the PSF exhibits prominent wings at distances $\gtrsim 10$ arcsec, being more pronounced in the $i$ band than in the $g$ and $r$ filters (Bergval, Zaricksson & Caldwell 2010). If neglected, the wings in the redder bands of the PSF cause a spurious red colour excess (in $g-i$ and $r-i$) in the galaxy outskirts (de Jong 2008; TvD11). Our colour profiles are based on PSF-corrected structural parameters. The PSF is obtained by fitting images of stars with a superposition of 2D Moffat functions, truncated at a maximum radius, $r_{PSF}$, where the PSF model reaches a mean flux level of 1 per cent of its central value. In the previous papers of the SPIDER survey, $r_{PSF}$ is typically $\sim 7$ pixels (i.e. $\sim 2.8$ arcsec) in all wavebands. This issue is not relevant for those papers, as only the properties within 1–2 effective radii were considered. However, when studying the profiles out to $8R_e$, this choice will underestimate the effect of the wings of the PSF. To account for this, we have reprocessed the *griz* images of all the 674 selected ETGs using a large PSF model, with $r_{PSF} = 60$ pixels ($\sim 24$ arcsec). Hereafter, we refer to the original ($r_{PSF} = 7$ pixels) and the updated PSF models as the small and large PSFs, respectively. Fig. 3 compares the median-stacked $g-r$, $g-i$ and $g-z$ colour profiles of high-mass ETGs with respect to the size of the PSF model. Using a small PSF makes the galaxy colour redder in the external regions, beyond $\sim 1\,R_e$, in agreement with de Jong (2008) and TvD11. As expected from the waveband dependence of the PSF halo (see fig. 6 of Bergval et al. 2010), the effect is stronger in $g-i$ (and $g-z$) than in $g-r$. In the inner regions, at $R/R_e < 1$, the profiles (and hence the inner colour gradients) are not affected by the choice of PSF model. For the analysis presented in this paper, we have obtained all optical colour profiles using the large PSF. Notice that UKIDSS PSFs are not affected from any extended wing, as oppose to the $i$- and $z$-band (SDSS) PSFs. Also, the large wavelength baseline probed by optical–NIR colours makes them insensitive to any PSF red halo effect. For this reason, we have decided not to

Downloaded from https://academic.oup.com/mnras/article/426/3/2300/988992 by guest on 06 June 2022

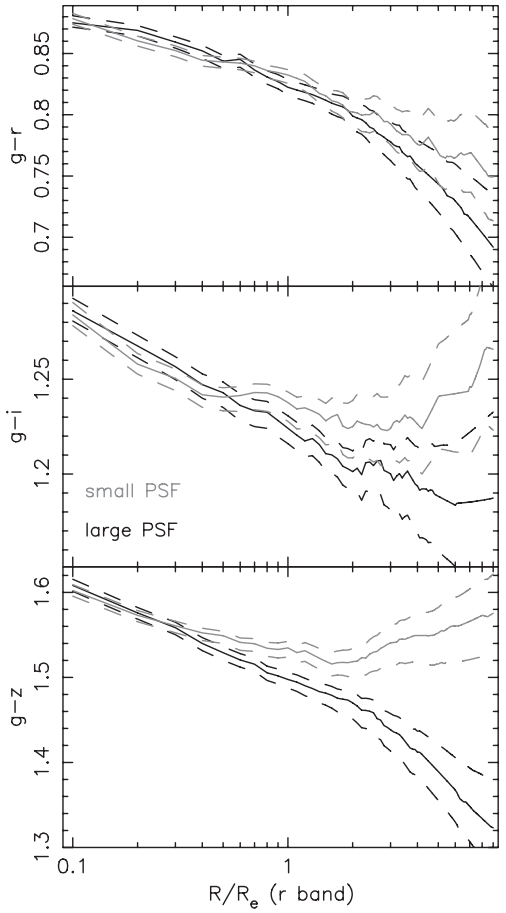



**Figure 3.** Comparison of $g - r$, $g - i$ and $g - z$ colour profiles, when using a small ($r_{PSF} = 2.8$ arcsec, grey curves) and large ($r_{PSF} = 24$ arcsec, black curves) PSF model (see text for details). Solid curves mark median trends, while dashed curves are the $\pm 1\sigma$ uncertainties on the median.

reprocess the NIR wavebands, and use the Sérsic profiles from our previous works.

## 4 COLOUR PROFILES VERSUS GALAXY MASS

Fig. 4 plots the median colour profiles, $g - X$ (with $X = rizYJHK$), obtained by median-stacking the single profiles of all galaxies in each of the three stellar mass bins. For each panel, the black dashed line represents the slope of the colour profile in the radial range from 0.1 to 1 $R_e$, i.e. the average colour gradient, $\nabla_{g-X}$, as estimated in Paper IV. Error bars are $1\sigma$ uncertainties on median colours, for intermediate-mass ETGs, at different fiducial galactocentric distances, i.e. $R/R_e = \{0.1, 0.5, 1, 2, 4, 8\}$. The values of 0.1 and 1 $R_e$ define the range usually adopted to estimate internal colour gradients of ETGs (e.g. Peletier et al. 1990), while the distances $\{2, 4, 8\}$ $R_e$ are chosen to analyse the behaviour of colour gradients in the outermost regions. We adopt a maximum radius of $8R_e$, so that the photometric errors are kept small enough ($\lesssim$0.04 mag) to allow for a meaningful SP analysis (Section 5.2). Moreover, as noticed above, a single Sérsic model might not be able to describe the light content of ETGs at larger galactocentric distances (TvD11). The median $g - X$ colours (with $X = rizYJHK$), computed at the fiducial galactocentric distances, are reported, together with their uncertainties, in Tables 1–3, for low-, intermediate- and high-mass ETGs, respectively. Notice that both the median $g - X$ colours and colour uncertainties are obtained by stacking the parametric colour profiles (equation 2).

Both optical–optical and optical–NIR colour profiles become bluer towards the galaxy outskirts, up to $\sim 8R_e$. Overall, with the exception of $g - r$ and $g - J$, the profiles are reasonably linear over the entire log-radial range. In $g - i$, low- and intermediate-mass galaxies exhibit some deviation from the linear trend at $R/R_e \gtrsim 3$, perhaps reflecting some inaccuracy in the $i$-band PSF halo modelling at large distances. However, the deviation is comparable to the size of the error bars, making the effect unimportant for the SP analysis (Section 5.2). The curvature in the $g - r$ profiles is small, considering error bars, while the $g - J$ profile shows a strong curvature, not seen in other optical–NIR colours ($g - Y$, $g - H$ and $g - K$). This might be explained by systematics in the $J$-band structural parameters, due to the different quality and resolution of the $J$-band photometry (see Paper I for more details). For this reason, we do not use $g - J$ to constrain radial trends of stellar properties (Section 5.2).

This paper constitutes the first comprehensive analysis of optical–optical and optical–NIR colours, as a function of galaxy mass, out to the halo region of ETGs ($8R_e$). On the other hand, for what concerns optical data alone, we can compare our results with those obtained by TvD11, whose analysis was based on stacking a large sample of 42 000 luminous red galaxies from SDSS, at redshift $z \sim 0.34$. Fig. 5 compares our $g - r$ colour profile, for high-mass ETGs, with their $r - i$ stacked profile. Notice that, at $z \sim 0.34$, the $r - i$ colour roughly corresponds to $g - r$ in the rest frame, allowing for a direct comparison to our colour profiles. The $r - i$ profile has been extracted from fig. 8 of TvD11 (left-hand panel) and normalized to match our average $g - r$ within $R_e$. Our profile and that of TvD11 are in very good agreement within an effective radius, while at large distances, the TvD11 stacked data appear slightly bluer (by $\sim$0.03 mag), but fully consistent with our results, considering error bars and the different selection criteria (e.g.. redshift range) of our and TdV11 samples.

## 5 CONSTRAINING THE PROPERTIES OF THE UNDERLYING STELLAR POPULATIONS

### 5.1 Stellar population models

We compare the observed colours of ETGs with the predictions of three different versions of a well-established SP synthesis code: (a) the BC03 models; (b) the minor revision of these models introduced by Charlot & Bruzual (2007, henceforth CB07) and (c) the major revision of this code and models in preparation by Charlot & Bruzual (in preparation, hereafter CB*). The CB07 models use the same sets of stellar tracks and spectral libraries as the BC03 models (see BC03 for details), except for the thermally pulsing asymptotic giant branch (TP-AGB) stars. For these stars, CB07 follow the semi-empirical evolutionary prescriptions by Marigo & Girardi (2007) and Marigo et al. (2008). The CB* population synthesis models used in this paper are based on the stellar evolution models computed with updated input physics for stars up to 15 $M_\odot$ by Bertelli et al. (2008). These tracks are available for metallicities $Z = \{0.0001, 0.0004, 0.001, 0.002, 0.004, 0.008, 0.017, 0.04, 0.07\}$, with the solar metallicity being $Z_\odot = 0.017$. In CB* the evolution of TP-AGB stars follows a recent prescription by Marigo & Girardi (private communication), which has been calibrated using observations of AGB stars in the Magellanic Clouds and nearby galaxies (Girardi et al. 2010; Melbourne et al. 2012). In the optical range, the CB*

Downloaded from https://academic.oup.com/mnras/article/426/3/2300/988992 by guest on 06 June 2022

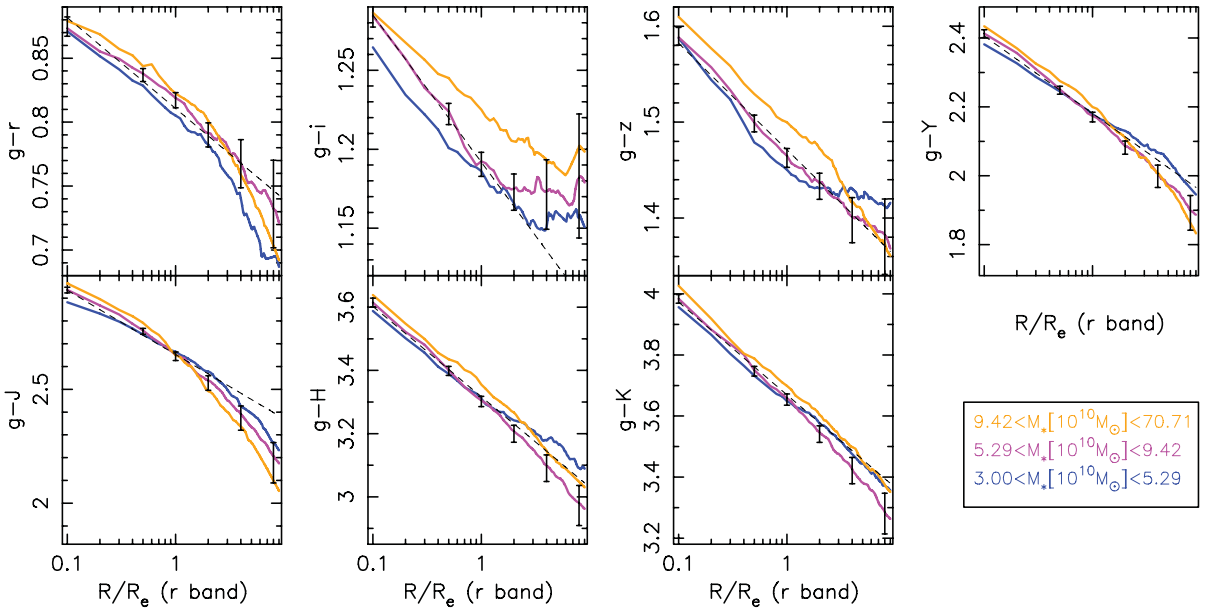



**Figure 4.** Median colour profiles, in the form of $g - X$ (with $X = rizYJHK$), for the sample of 674 ETGs, as a function of the normalized galactocentric distance $R/R_e$. For each panel, the blue, magenta and orange curves are the median profiles for galaxies in the same stellar mass bins, as labelled (see bottom-right of the figure). The black dashed lines have slopes equal to the peak values of colour gradient distributions of SPIDER ETGs, as reported in table 2 of Paper IV. The intercept of the dashed lines has been arbitrarily chosen to match the inner ($R < R_e$) colour profile of intermediate-mass galaxies (magenta curve). The six vertical error bars mark the positions of 0.1, 0.5, 1, 2, 4, 8 effective radii that we select to analyse the variation of colour gradients in ETGs from their centre to the outskirts. The size of the error bars is given by the $\pm 1\sigma$ error on the median colour profile of intermediate-mass galaxies (magenta colour). Notice the remarkable upturn in the $g - i$ and $g - z$ profiles at $R \gtrsim R_e$ for intermediate- and high-mass galaxies.

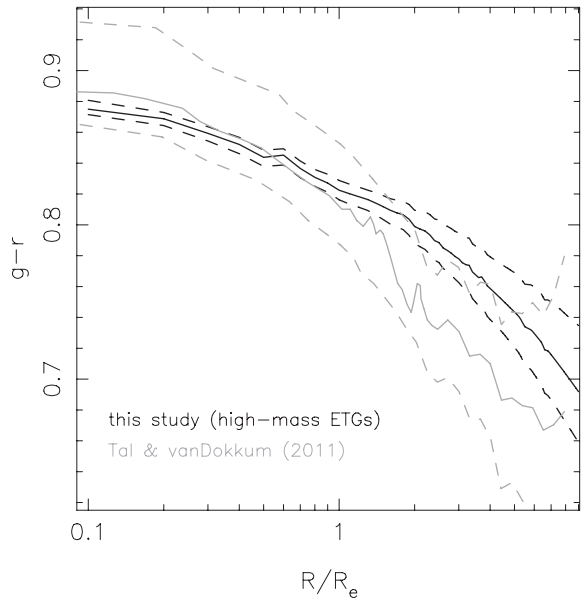



**Figure 5.** Comparison of our $g - r$ stacked colour profile with the $r - i$ stacked profile obtained for ETGs at redshift $z \sim 0.34$ by TvD11. Notice that at $z \sim 0.34$ the $r - i$ colour corresponds approximately to $g - r$ in the rest frame. The TvD11 profile matches well our colour profile in the inner galaxy region ($R < R_e$), while at larger radii their profile appears bluer (by $\sim$0.03 mag), although fully consistent within the error bars, with our results.

models are available for the IndoUS (Valdes et al. 2004), Miles (Sánchez-Blázquez et al. 2006a), Stelib (Le Borgne et al. 2003) and BaSeL 3.1(Westera et al. 2002) spectral libraries. The NIR spectra of TP-AGB stars in CB* are selected from the compilation by Lançon & Mouhcine (2002), the NASA Infrared Telescope Facility (IRTF) library (Rayner et al. 2009) and the C-star model atlas by Aringer et al. (2009). For stars of metallicity near $Z_\odot$, the number of available stellar spectra in the IndoUS and Miles libraries increases by a factor of roughly 20 with respect to the Stelib library used in BC03. Thus, in both metallicity and spectral coverage, the CB* models represent a major improvement over the BC03 models, which translate into a better modelling of the NIR and optical galaxy colours.

**Table 4.** SP synthesis models adopted in the present study.

| Model | Stellar library | IMF |
|---|---|---|
| BC03 | STELIB | Scalo |
| CB07SC | STELIB | Chabrier |
| CB*IC(CB*IS) | INDOUX | Chabrier (Salpeter) |
| CB*MC(CB*MS) | MILES | Chabrier (Salpeter) |
| CB*SC(CB*SS) | STELIB | Chabrier (Salpeter) |
| CB*BC(CB*BS) | BaSel 3.1 | Chabrier (Salpeter) |

Recently, it has become clear that the treatment of the TP-AGB stars in the CB07 models tends to overestimate the contribution by these stars in the NIR (Kriek et al. 2010; Melbourne et al. 2012; Zibetti et al. 2012). We use the CB07 models in this paper for the sake of completeness and comparison with previous work (e.g. La Barbera & de Carvalho 2009; Paper IV).

The simple stellar population (SSP) models adopted in the present study, and the labels we use to refer to them, are summarized in Table 4. The IMFs used are Scalo (BC03) and Chabrier (CB07), while we consider both Chabrier and Salpeter[1] (1955) IMF, for

[1] That is, a power-law IMF with slope 1.35, and lower and upper mass cut-offs of 0.1 and 100 $M_\odot$, respectively.

Downloaded from https://academic.oup.com/mnras/article/426/3/2300/988992 by guest on 06 June 2022

CB*. Models in the metallicity range between 1/50 and 2.5 $Z_\odot$ are considered, in the age range from 1 to 18 Gyr. The lower age limit of 1 Gyr is because we study ETGs, dominated by old SP, while the upper limit of 18 Gyr is the maximum age value available in the models.[2]

For a given model, synthetic colours are computed for three different star formation histories:

(i) *Simple Stellar Population.* Equivalent to an instantaneous burst of star formation.

(ii) $\tau$ *models.* We assume an exponentially declining star formation rate with e-folding time $\tau$. The age of the model (i.e. the first epoch of star formation) and its metallicity are in the same ranges as for the SSPs. The $\tau$ is varied from zero to the age of the model.

(iii) *Burst model.* The star formation rate is constant, with duration $\Delta t$. The age and metallicity of the model are varied in the same ranges as for $\tau$ models. $\Delta t$ is varied from zero to the age of the model.

To compute synthetic colours, $(g-X)_{\rm MOD}$ ($X = rizYHK$, see below), each SP model is converted to the median redshift of ETGs in our sample ($z = 0.0614$), and integrated with the $grizYHK$ throughput curves (see Paper I for details).

### 5.2 Colour fitting

For a given galaxy mass bin, and given galactocentric distance, we fit the corresponding median colours of ETGs by minimizing the following expression:

$$\chi^2 = \sum_X \frac{[(g-X)_{\rm OBS} - (g-X)_{\rm MOD} + OFF_X]^2}{\sigma^2_{g-X}}, \qquad (3)$$

where the summation extends over the available filters ($X = rizYHK$), and the subscripts *OBS* and *MOD* refer to observed (Tables 1–3) and synthetic (model) colours (see Section 5.1), respectively. The terms $OFF_X$ ($X = rizYHK$) are photometric zero-point offsets, adopted to improve the data and model matching (see below). In practice, the minimization consists of searching for the set of SP parameters (e.g. the age and metallicity for SSP models) that minimize equation (3). We remind the reader that $g-J$ colours are not used in the minimization procedure, for the reasons explained in Section 4. Because some model parameters are intrinsically degenerate when fitting broad-band colours (e.g. the formation epoch and $\tau$, or $\Delta t$), for each model we give only the mass-weighted age parameter (*Age*, hereafter simply referred to as the age of the model), and metallicity ($Z$) and analyse how these quantities change with galaxy mass and galactocentric distance. This allows us to verify how the assumption of a given SFR affects the estimate of age and metallicity profiles in ETGs.

The terms $OFF_X$ in equation (3) depend only on the adopted SP synthesis code (although the dependence is small, see below), and account for the fact that, in general, model colours do not match exactly the observed colours, because of, for example, uncertainties in the photometric calibration and/or SP synthesis ingredients. To illustrate this point, we consider CB*MC models and plot in Fig. 6 the $R = 1\,R_e$ colours of low-, intermediate- and high-mass ETGs. For a clearer figure including all colours in the same plot, we have subtracted the median colours, $\langle g-X\rangle$, the medians being computed among all mass bins and galactocentric distances. The values of both $\langle g-X\rangle$ and $OFF_X$, for SSP models from different synthesis codes, are reported in Table 5. Dotted curves in Fig. 6 are obtained for CB07SC SSP models by minimizing equation (3) with the values of $OFF_X$ set to zero. Notice the significant difference between observed and (best-fitting) model colours, ranging from a few hundredths of magnitude ($g-r$ and $g-K$) up to ∼0.1 mag in $g-Y$. To derive the offsets, $OFF_X$, we set $OFF_X = 0$ in equation (3), and fit the observed colours with a given set of models (e.g. SSPs), for each galaxy mass bin and galactocentric distance. The values of $OFF_X$ are defined as the median differences of all observed and best-fitting colours. After including the $OFF_X$ terms in equation (3), and repeating the minimization procedure, we find that the median differences of observed and best-fitting colours become smaller than ∼0.007 mag, proving that the entire procedure is self-consistent. We note that by using $\tau$ and burst (rather than simple) SP models, the offsets change less than ∼0.01 mag, while the offsets differ by $\lesssim$0.03 mag for SSPs among different SP codes (see Table 5). The dashed curves in Fig. 6 show the offset-corrected model colours, i.e. $(g-X)_{\rm MOD} - OFF_X$, hereafter simply referred to as best-fitting model colours. Notice how the matching of observed and model colours improves significantly when applying the offsets. Fig. 7 plots, as an example, the observed colours at all fiducial galactocentric distances (see Section 3), for low-, intermediate- and high-mass galaxies, and corresponding best-fitting colours for CB*MC SSPs. Overall, we find that all the adopted models (i.e.

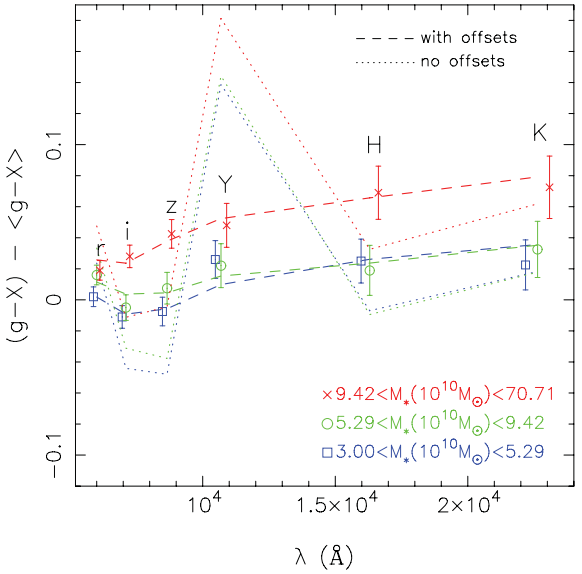



**Figure 6.** The median colours of ETGs, computed at $R = R_e$, are plotted in the form of $(g-X) - \langle g-X\rangle$ (with $X = rizYHK$) as a function of the typical wavelength of filter $X$, where $\langle g-X\rangle$ is the median of all $g-X$ values at different galaxy radii and masses (Tables 1–3). Different symbols refer to galaxies with different mass, as indicated in the lower-right of the plot. Error bars are $1\sigma$ uncertainties on median colours. Dotted curves are the best-fitting SSP models from CB*MC (see text). Notice the discrepancy between models and data. The dashed curves are best-fitting SSP models after suitable correction offsets ($OFF_X$) were applied, improving the matching between models and data.

[2] We do not set the age of the Universe as an upper limit for the present analysis, as the absolute matching of model and observations is still very uncertain. In fact, large differences exist between best-fitting ages from different models (see Section 6.1), while relative differences in age and metallicity (i.e. the radial gradients) are much better constrained.



Downloaded from https://academic.oup.com/mnras/article/426/3/2300/988992 by guest on 06 June 2022

**Table 5.** Median colours of ETGs and photometric offsets, $OFF_X$, applied to different SSP models. For CB* models, the offsets corresponding to a Salpeter (S), rather than Chabrier (C), IMF are given in brackets.

| *Colour* | *Median* | $OFF_X$ | | | | | |
|---|---|---|---|---|---|---|---|
| | | BC03 | CB07SC | CB*IC(S) | CB*MC(S) | CB*SC(S) | CB*BC(S) |
| $g-r$ | 0.803 | −0.033 | −0.019 | −0.028(−0.027) | −0.022(−0.022) | −0.025(−0.022) | −0.016(−0.018) |
| $g-i$ | 1.197 | 0.032 | 0.031 | 0.028(0.029) | 0.035(0.034) | 0.024(0.023) | 0.039(0.039) |
| $g-z$ | 1.458 | 0.044 | 0.016 | 0.054(0.052) | 0.042(0.034) | 0.049(0.044) | 0.023(0.018) |
| $g-Y$ | 2.152 | −0.119 | −0.131 | −0.109(−0.114) | −0.129(−0.132) | −0.117(−0.121) | −0.131(−0.131) |
| $g-H$ | 3.286 | 0.035 | 0.060 | 0.016(0.018) | 0.033(0.040) | 0.028(0.032) | 0.044(0.045) |
| $g-K$ | 3.627 | 0.037 | 0.041 | 0.014(−0.011) | 0.017(0.027) | 0.017(0.024) | 0.025(0.034) |

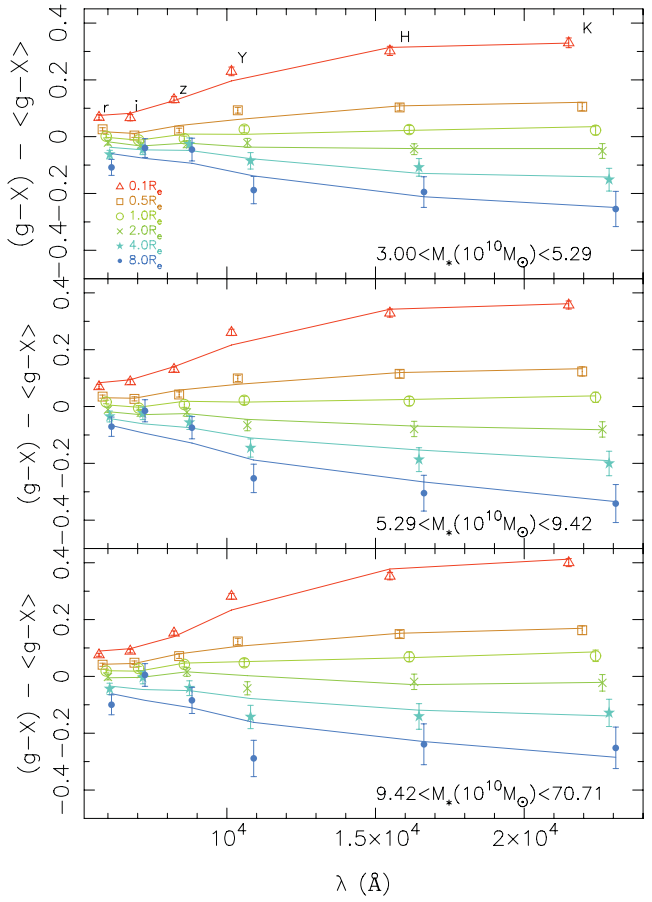



**Figure 7.** The colours used in this paper ($g-X$) are shown as a function of the effective wavelength of filter $X$. Top, middle and bottom panels correspond to low-, intermediate-, and high-mass galaxies, respectively. For each mass bin, different galactocentric distances, $R/R_e = \{0.1, 0.5, 1, 2, 4, 8\}$, are plotted with different colours and symbols (see lower-left of top panel). The curves are best-fitting SSP colours for CB*MC models. Notice the good matching of observed and model colours.

population synthesis codes and star formation histories) provide a fairly good match to the observations in all available passbands (but for $J$ band, see above). We characterize the quality of colour fitting by computing the median rms value of differences between best-fitting and observed colours, the median being computed among all fiducial radii. These rms values are summarized, for all colour fits performed in the present work, in Table 6. Notice that the typical rms amounts to ∼0.02 mag. For what concerns best-fitting age and metallicity, averaging over all radial bins and all models, the (absolute) values of age (metallicity) differ by ∼18 per cent (14 per cent)

**Table 6.** Median rms of differences between best-fitting and observed colours, for all models and samples analysed in this work. The median values are computed among all fiducial radii, and inform on the quality of the colour fitting. For CB* models, the offsets corresponding to a Salpeter (S), rather than Chabrier (C), IMF are given in brackets.

| Model | Median rms | | |
|---|---|---|---|
| | Low mass | Intermediate mass | High mass |
| BC03 SSPs | 0.017 | 0.015 | 0.008 |
| CB07SC SSPs | 0.016 | 0.020 | 0.013 |
| CB*IC (CB*IS) SSPs | 0.022(0.020) | 0.017(0.012) | 0.019(0.019) |
| CB*MC (CB*MS) SSPs | 0.032(0.016) | 0.010(0.010) | 0.015(0.015) |
| CB*SC (CB*SS) SSPs | 0.015(0.015) | 0.014(0.015) | 0.014(0.012) |
| CB*BC (CB*BS) SSPs | 0.019(0.016) | 0.013(0.011) | 0.024(0.022) |
| CB*SC $\tau$ models | 0.016 | 0.015 | 0.014 |
| CB*SC burst models | 0.016 | 0.015 | 0.013 |
| CB07SC ($E(B-V)=0.04$) | 0.026 | 0.024 | 0.021 |
| CB07SC ($E(B-V)=0.08$) | 0.023 | 0.019 | 0.020 |
| CB07SC (for field ETGs) | 0.020 | 0.019 | 0.026 |
| CB*MC (for field ETGs) | 0.015 | 0.017 | 0.024 |
| CB07SC (for group ETGs) | 0.019 | 0.021 | 0.020 |
| CB*MC (for group ETGs) | 0.012 | 0.020 | 0.017 |

when (i) one applies the offsets and (ii) the values of $OFF_X$ are set to zero. On the other hand, relative values of age and metallicity (i.e. the gradients; see Section 6) are virtually unaffected by the value of $OFF_X$. In order to estimate uncertainties on best-fitting age and metallicity, we perform 200 bootstrap iterations, where, each time, observed colours are shifted according to their errors and the entire minimization procedure is repeated. This bootstrap procedure provides a joint probability distribution function (PDF) for age and metallicity. Confidence intervals on age and metallicity are obtained at the $1\sigma$ equivalent, by computing the 16th and 84th percentiles of the marginalized PDF.

## 6 AGE AND METALLICITY GRADIENTS OUT TO $8\,R_e$

### 6.1 SSP models

Fig. 8 plots the best-fitting age and metallicity as a function of galactocentric distance, for BC03, CB07 and CB* (Chabrier IMF) SSP models. In the radial range from 0.1 to 1 $R_e$, the *Age* parameter (i.e. the 'SSP-equivalent' age) increases, while metallicity decreases, implying that ETGs have negative metallicity gradients and positive age gradients, consistent with previous findings (e.g. McClure 1969; Peletier et al. 1990; Gorgas, Efstathiou & Aragón-Salamanca 1990; Gonzalez 1993; Davies et al. 1993; Ferreras et al. 2005, 2009a; Sánchez-Blázquez, Gorgas & Cardiel 2006b; Clemens et al.

Downloaded from https://academic.oup.com/mnras/article/426/3/2300/988992 by guest on 06 June 2022

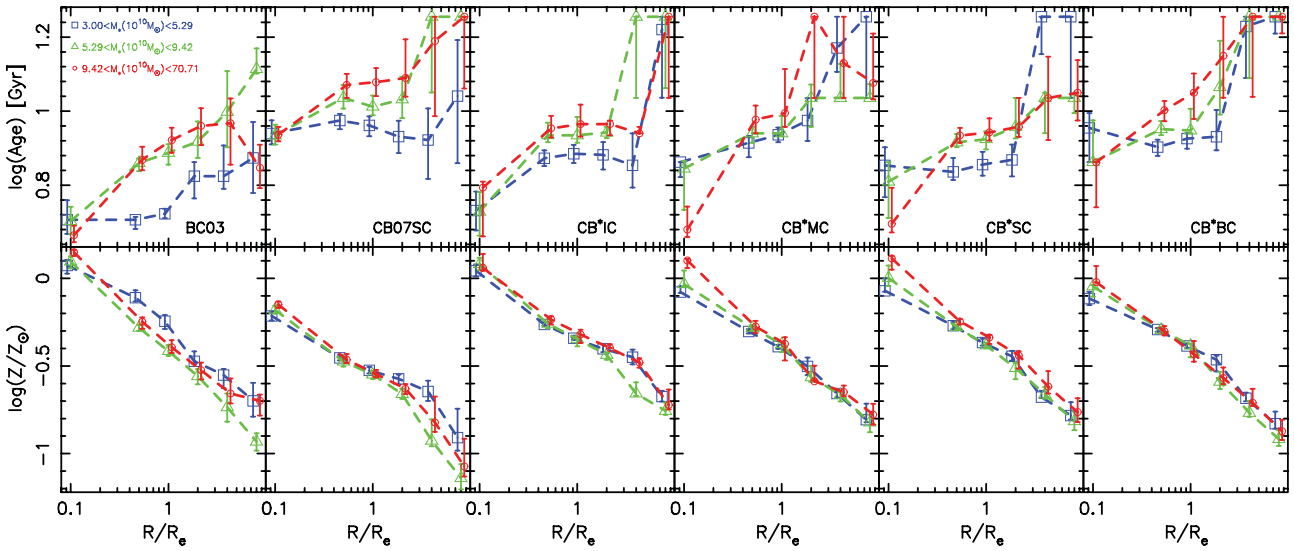



**Figure 8.** Age and metallicity profiles obtained by fitting galaxy colours with SSP models, as a function of galactocentric distance, for low-(blue), intermediate-(green), and high-(red) mass ETGs. Different symbols are used for different galaxy mass bins, as illustrated in the top-left panel. From left to right, top and bottom panels refer to different models (BC03, CB07SC, CB*IC, CB*MC, CB*SC, CB*BC), as illustrated by the black labels in the top panels. All models correspond to a Chabrier IMF. Error bars denote the 16th and 84th percentile uncertainties (corresponding to $1\sigma$ errors for a normal deviate) on best-fitting age and metallicity.

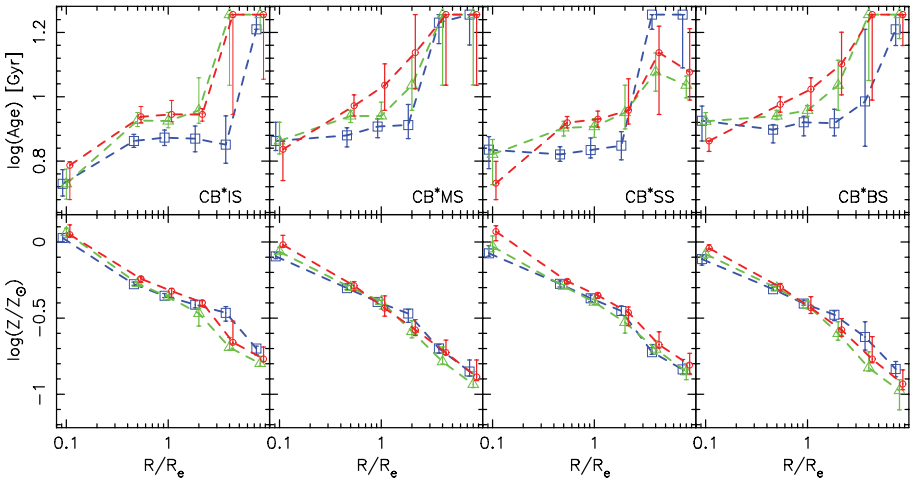



**Figure 9.** Same as Fig. 8 but plotting only the results for the CB* models using a Salpeter IMF.

2009; La Barbera & de Carvalho 2009; Suh et al. 2010; Tortora et al. 2010). In the present study, we supersede previous works, by exploring, for the first time, the behaviour of age and metallicity at large galactocentric distances. Overall, we find that at $R > R_e$, *Age* keeps increasing, while metallicity decreases, out to $\sim 8R_e$. Notice that the error bars on *Age* are on average large (up to 40 per cent for some models and mass bins) at $R > R_e$, reflecting the uncertainties on galaxy colours, as well as the fact that 'old' (i.e. $\gtrsim$4 Gyr) ages are intrinsically more difficult to constrain. This is due to the fact that for an old SP, a variation in age does not change much the model colours. Hence, the large uncertainties on *Age* at $R > R_e$ do not significantly affect those in metallicity, which remain reasonably small (<10–20 per cent) even at large galactocentric distances. Furthermore, the radial trend with metallicity appears quite robust across the different population synthesis models considered. Fig. 9 shows the age and metallicity profiles for CB* models when using a Salpeter IMF. Overall, the profiles are very similar to those presented in Fig. 8, implying that the choice of IMF in the SP models does not change at all our conclusions.

In order to quantify the change in the slopes of the age and metallicity profiles, i.e. the age and metallicity gradients (hereafter $\nabla_t$ and $\nabla_Z$), as a function of radius, we perform an orthogonal linear regression of the profiles in the inner [$\log(R/R_e) \leq 0$] and outer [$\log(R/R_e) > 0$] regions separately. The slopes give the inner and outer metallicity gradients ($\nabla_{Z,i}$ and $\nabla_{Z,o}$), and the inner age gradient ($\nabla_{t,i}$). Since age profiles become noisier at $R > R_e$, we do not perform any fit of the *Age* profile in the outskirts. Instead, we compute the average, logarithmic difference in *Age*, $\Delta_t$, between the outer region[3] ($R > 1\,R_e$) and the galaxy centre ($R = 0.1\,R_e$). In

[3] In practice, we compute the mean value of *Age* among the three fiducial radii of 2, 4 and 8 $R_e$, and then take the logarithmic difference between this mean value and the *Age* at $R = 0.1\,R_e$.



Downloaded from https://academic.oup.com/mnras/article/426/3/2300/988992 by guest on 06 June 2022

**Table 7.** Metallicity gradients ($\nabla_Z$) of ETGs estimated using different SSP models. Subscript $i$ and $o$ refer to the inner ($R \leq R_e$) and outer ($R_e < R \leq 8R_e$) radial ranges where the gradients are estimated.

| Model | Metallicity gradients | | | | | |
|---|---|---|---|---|---|---|
| | $\nabla_{Z,i}$ | | | $\nabla_{Z,o}$ | | |
| | Low mass | Intermediate mass | High mass | Low | Intermediate | High mass |
| BC03 | $-0.31 \pm 0.06$ | $-0.52 \pm 0.05$ | $-0.55 \pm 0.04$ | $-0.38 \pm 0.17$ | $-0.62 \pm 0.12$ | $-0.29 \pm 0.12$ |
| CB07SC | $-0.32 \pm 0.04$ | $-0.38 \pm 0.03$ | $-0.41 \pm 0.03$ | $-0.57 \pm 0.26$ | $-0.80 \pm 0.13$ | $-0.74 \pm 0.20$ |
| CB*IC | $-0.40 \pm 0.04$ | $-0.44 \pm 0.05$ | $-0.39 \pm 0.05$ | $-0.46 \pm 0.06$ | $-0.54 \pm 0.07$ | $-0.55 \pm 0.12$ |
| CB*MC | $-0.30 \pm 0.04$ | $-0.35 \pm 0.05$ | $-0.49 \pm 0.07$ | $-0.58 \pm 0.14$ | $-0.43 \pm 0.10$ | $-0.32 \pm 0.13$ |
| CB*SC | $-0.29 \pm 0.05$ | $-0.39 \pm 0.07$ | $-0.46 \pm 0.05$ | $-0.57 \pm 0.09$ | $-0.50 \pm 0.12$ | $-0.54 \pm 0.15$ |
| CB*BC | $-0.27 \pm 0.03$ | $-0.34 \pm 0.06$ | $-0.41 \pm 0.07$ | $-0.61 \pm 0.12$ | $-0.54 \pm 0.11$ | $-0.51 \pm 0.13$ |
| CB*IS | $-0.39 \pm 0.03$ | $-0.43 \pm 0.04$ | $-0.38 \pm 0.06$ | $-0.49 \pm 0.07$ | $-0.55 \pm 0.13$ | $-0.62 \pm 0.08$ |
| CB*MS | $-0.30 \pm 0.03$ | $-0.33 \pm 0.03$ | $-0.41 \pm 0.08$ | $-0.64 \pm 0.13$ | $-0.58 \pm 0.13$ | $-0.51 \pm 0.13$ |
| CB*SS | $-0.29 \pm 0.05$ | $-0.37 \pm 0.05$ | $-0.43 \pm 0.06$ | $-0.65 \pm 0.10$ | $-0.54 \pm 0.13$ | $-0.58 \pm 0.16$ |
| CB*BS | $-0.29 \pm 0.03$ | $-0.33 \pm 0.03$ | $-0.39 \pm 0.06$ | $-0.59 \pm 0.11$ | $-0.63 \pm 0.20$ | $-0.59 \pm 0.16$ |

**Table 8.** Same as Table 7 but for age, rather than metallicity, gradients ($\nabla_t$). Notice that instead of computing age gradients in the galaxy outskirts, we measure the mean logarithmic age difference, $\Delta_t$, between the outer radial range and the galaxy centre (see text for details).

| Model | Age gradients | | | | | |
|---|---|---|---|---|---|---|
| | $\nabla_{t,i}$ | | | $\Delta_t$ | | |
| | Low mass | Intermediate mass | High mass | Low mass | Intermediate mass | High mass |
| BC03 | $0.01 \pm 0.03$ | $0.19 \pm 0.03$ | $0.26 \pm 0.02$ | $0.13 \pm 0.06$ | $0.31 \pm 0.05$ | $0.26 \pm 0.04$ |
| CB07SC | $0.03 \pm 0.03$ | $0.09 \pm 0.02$ | $0.15 \pm 0.02$ | $0.03 \pm 0.08$ | $0.25 \pm 0.05$ | $0.24 \pm 0.07$ |
| CB*IC | $0.16 \pm 0.03$ | $0.22 \pm 0.04$ | $0.18 \pm 0.06$ | $0.25 \pm 0.08$ | $0.42 \pm 0.08$ | $0.26 \pm 0.10$ |
| CB*MC | $0.04 \pm 0.04$ | $0.10 \pm 0.05$ | $0.34 \pm 0.05$ | $0.28 \pm 0.07$ | $0.19 \pm 0.09$ | $0.47 \pm 0.08$ |
| CB*SC | $-0.00 \pm 0.05$ | $0.12 \pm 0.06$ | $0.26 \pm 0.05$ | $0.27 \pm 0.09$ | $0.20 \pm 0.09$ | $0.32 \pm 0.09$ |
| CB*BC | $-0.04 \pm 0.05$ | $0.09 \pm 0.05$ | $0.19 \pm 0.06$ | $0.18 \pm 0.08$ | $0.33 \pm 0.08$ | $0.36 \pm 0.10$ |
| CB*IS | $0.15 \pm 0.05$ | $0.21 \pm 0.05$ | $0.17 \pm 0.09$ | $0.25 \pm 0.05$ | $0.43 \pm 0.07$ | $0.37 \pm 0.10$ |
| CB*MS | $0.04 \pm 0.06$ | $0.08 \pm 0.06$ | $0.20 \pm 0.09$ | $0.27 \pm 0.06$ | $0.32 \pm 0.09$ | $0.38 \pm 0.10$ |
| CB*SS | $-0.00 \pm 0.06$ | $0.09 \pm 0.08$ | $0.21 \pm 0.07$ | $0.28 \pm 0.06$ | $0.20 \pm 0.08$ | $0.33 \pm 0.09$ |
| CB*BS | $-0.01 \pm 0.06$ | $0.03 \pm 0.05$ | $0.16 \pm 0.05$ | $0.11 \pm 0.09$ | $0.26 \pm 0.07$ | $0.34 \pm 0.07$ |

contrast, errors on metallicity remain small even at large galactocentric distances (see above), allowing us to estimate meaningful outer metallicity gradients. Errors on $\nabla_t$, $\nabla_Z$ and $\Delta_t$ are estimated as the errors on age and metallicity (see the concluding part of Section 5.2), performing 200 bootstrap iterations, where colours are shifted according to their uncertainties, and age and metallicity gradients are re-estimated, by repeating the $\chi^2$ minimization procedure at each fiducial radius. For all different SSP models, the values of $\nabla_{Z,i}$ and $\nabla_{Z,o}$ ($\nabla_{t,i}$ and $\Delta_t$) are reported in Table 7 (Table 8).

Fig. 8 unsurprisingly shows that absolute estimates of *Age* and metallicity differ significantly among different models, while *relative* trends, i.e. with respect to mass and galactocentric distance, do not (but see below). In the galaxy centre ($R \sim 0.1\,R_e$), BC03 models predict a super-solar metallicity ($\sim 1.4\,Z_\odot$) and an *Age* of $\sim$5 Gyr, while for CB07, the central metallicity is sub-solar ($\sim 0.65\,Z_\odot$), and *Age* older (with respect to BC03) by $\sim$4 Gyr. The new CB* models also exhibit significant reciprocal differences in *Age* (up to a few Gyr), and relatively small differences in $Z$ ($\sim$0.1 dex), when comparing results based on different stellar libraries (CB*IC; CB*MC; CB*SC; CB*BC). Notice that, for high-mass ETGs, all CB* models predict either solar (CB*MC; CB*BC) or super-solar (CB*IC; CB*SC) metallicities. Hence, in contrast to the CB07 models, the photometric constraints of the CB* models are more consistent with the results from spectroscopic studies of the central regions of ETGs (e.g. Gallazzi et al. 2006; Pasquali et al. 2010). Since the absolute *Age* is strongly model dependent (even when changing only the adopted stellar library in CB*), we have not set the age of the Universe as an upper limit for the models (see Section 5.1), and several profiles in Fig. 8 keep increasing outwards up to the maximum allowed value of 18 Gyr. Imposing an *Age* upper limit of 13.75 Gyr (i.e. the current best estimate for the age of the Universe; Komatsu et al. 2011) would produce an upper cut-off in the *Age* profiles, while not affecting significantly the metallicity profiles. Considering the large *Age* differences among different models, enforcing an upper limit on *Age* is not meaningful for the models, so we decided not to apply this constraint.

Overall, the key features of the age and metallicity trends are summarized as follows.

(i) Metallicity is a monotonic, decreasing function of galactocentric distance in ETGs, out to (at least) $8R_e$. This is the most robust result, holding true for all mass bins, and for all different models probed here.

(ii) The values of $\Delta_t$ in Table 8 are always positive. In most cases (and in particular for all CB* models with Chabrier IMF), this result is found above the $2\sigma$ level. For high-mass galaxies, the $\Delta_t$ is positive at more than the $3\sigma$ level for all models. We conclude that ETGs, in particular the most massive ones, host significantly older SPs in their haloes ($R \gtrsim$ a few $\times\, R_e$) than in their cores.

(iii) In the inner region, the metallicity gradient, $\nabla_{Z,i}$, steepens at high mass, while $\nabla_{t,i}$ increases with $M_\star$. These trends hold for

Downloaded from https://academic.oup.com/mnras/article/426/3/2300/988992 by guest on 06 June 2022

all models, except for CB*/IndoUS, where no mass dependence is detected. A steepening of $\nabla_{Z,i}$ and $\nabla_{t,i}$ with galaxy mass has also been found in previous papers based on the SPIDER survey (e.g. Paper IV; La Barbera et al. 2011, hereafter LF11), where colour gradients were fitted (rather than colours) with SP models. Notice that at high mass, the $\nabla_{t,i}$ is always positive, regardless of the SP model, consistent with our findings for $\Delta_t$ in the external regions. At intermediate and low mass, the $\nabla_t$ is either consistent with zero, within the errors, or significantly positive. In particular, at low mass, the age trend is flat for most models (i.e. BC03, CB07SC, CB*SC and CB*BC).

(iv) For low-mass ETGs, the metallicity gradient is steeper at large radii than in the centre, i.e. $\nabla_{Z,o} < \nabla_{Z,i}$. While this result holds for all models, it is statistically significant (at more than a 2–3$\sigma$ level) only for some models (e.g. CB*SC). At high mass, the same steepening is observed only for some models when using a Chabrier IMF (e.g. CB*IC), and for all models with a Salpeter IMF (in which case, however, the steepening is statistically significant only for CB*IS models). If a bottom-heavy, Salpeter-like, IMF is more appropriate for high-, relative to low-mass ETGs (e.g. van Dokkum & Conroy 2011; Cappellari et al. 2012), we might be tempted to conclude that the metallicity gradient of ETGs steepens at large galactocentric distances, independent of galaxy stellar mass.

### 6.2 Exponential and burst models

Fig. 10 shows radial trends of (mass-weighted) age and metallicity as obtained by fitting galaxy colours with composite SPs ($\tau$ and burst models). For brevity reasons, we only show one illustrative case, corresponding to CB*SC models (Section 5.2). Both *Age* and metallicity exhibit similar trends to those obtained with SSPs (Fig. 8). In particular, we see that (i) *Age* increases outwards, being oldest in the galaxy halo region; (ii) the age gradient is stronger (more positive) at higher galaxy mass, with low-mass ETGs having a flat age trend out to $\sim$2–4$R_e$; and (iii) metallicity decreases outwards, with a steeper (more negative) gradient (especially for low- and intermediate-mass galaxies) at large galactocentric distances. One may also notice that individual values of *Age* are somewhat more sensitive (in contrast to metallicity) to the adopted star formation history (i.e. SSP, $\tau$ and burst models). For instance, at $R > 3\,R_e$, and for low-mass ETGs, both burst and SSP models (see Fig. 8) give the oldest available *Age* (18 Gyr) in the input grid of values, while for $\tau$ models the *Age* is $\sim$13 Gyr (see blue curves in the upper panel of the figure). On the other hand, all models agree very well (within error bars) on the inferred value of metallicity at each radial position.

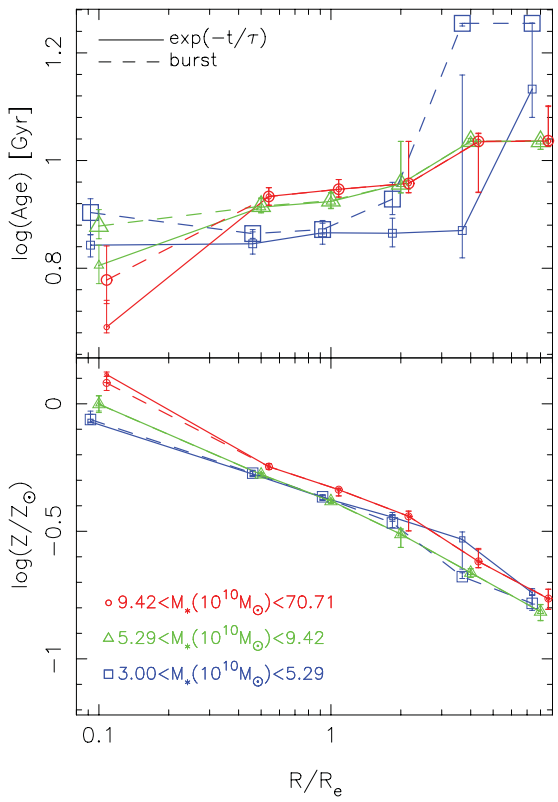



**Figure 10.** The best-fitting age (top) and metallicity (bottom) are shown as a function of galactocentric distance, as in Fig. 8, for low-(blue), intermediate-(green), and high-(red) mass ETGs. Smaller (larger) symbols and solid (dashed) curves refer to CB*SC exponentially declining (burst) models. Notice that the trends are very similar to those obtained with SSP models (Fig. 8).

### 6.3 Internal reddening

So far, we have neglected the role of internal reddening, which might mimic the presence of metallicity gradients in ETGs (Goudfrooij & de Jong 1995; Silva & Wise 1996; Wise & Silva 1996). Indeed, if dust gradients are present, a correlation of colour gradients and the amount of internal extinction should be detected. Such correlation does not exist but for a small fraction (<10 per cent) of ETGs in our sample (see Paper IV). Also, previous studies have found neither a significant correlation between colour gradients and Infrared Astronomical Satellite (IRAS) 100 μm flux (Michard 2005) nor a contribution of diffuse dust to the colour gradients (Savoy, Welch & Fich 2009). Although the evidence supports our assumption of neglecting extinction gradients in ETGs, the presence of uniform internal reddening inside the galaxies may still affect our conclusions, as it could bias the best-fitting values of age and metallicity at each radial position. To address this issue, we have applied dust extinction corrections to one of the available sets of CB* SSPs (CB*MC), adopting the Cardelli et al. (1989) extinction law, and repeated the SSP fitting procedure for two cases, i.e. a colour excess of $E(B-V) = 0.04$ and $E(B-V) = 0.08$. These values correspond to the median and the 75 per cent level of the probability distribution of the colour excess parameter, inferred by running the spectral fitting code STARLIGHT (Cid Fernandes et al. 2005), with the CB07SC models, on the SDSS spectra of our sample of ETGs (see Paper V for details). Fig. 11 shows the age and metallicity profiles obtained when adopting the above reddening values. The trends of age and metallicity are fully consistent with those obtained for the dustless models (see CB*MC profiles in Fig. 8).

### 6.4 Comparison with recent findings

Our findings (e.g. Fig. 8) can be compared with those of Coccato, Gerhard & Arnaboldi (2010, hereafter CGA10), who derived radial profiles of SP properties (i.e. SSP-equivalent age, [Z/H] and [$\alpha$/Fe]), based on spectroscopic data, for one of the two brightest galaxies in the Coma cluster (NGC 4889), out to a galactocentric distance of $\sim$4 $R_e$. CGA10 found that the SPs in the outer halo of NGC 4889 tend to be older than those in the inner regions, in agreement with our results. At $R \gtrsim 1.2\,R_e$, the metallicity profile of NGC 4889 flattens, while [$\alpha$/Fe] shows a steep negative gradient. Although the optical+NIR photometry allows us to reasonably disentangle the average contribution of age and metallicity to galaxy colours

Downloaded from https://academic.oup.com/mnras/article/426/3/2300/988992 by guest on 06 June 2022

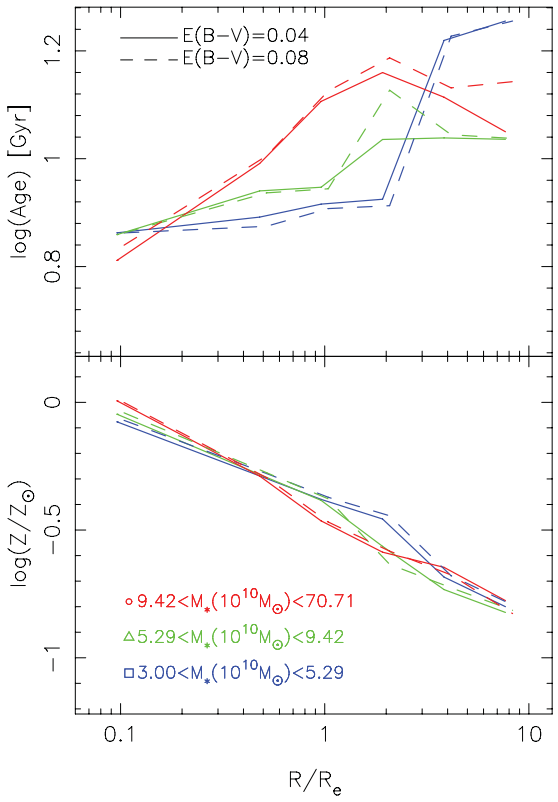



**Figure 11.** The same as right-hand panel of Fig. 8, but comparing results of CB07SC with Cardelli et al. (1989) extinction law applied, with a colour excess of $E(B-V) = 0.04$ (solid curves) and $E(B-V) = 0.08$ (dashed curves). Notice that internal reddening does not affect significantly the trends of age and metallicity with galactocentric distance.

(see Paper IV), we are not able to constrain both [Z/H] and [$\alpha$/Fe] separately, and our metallicity profiles can indeed be affected by radial changes of [$\alpha$/Fe].

For instance, the steepening of the metallicity profile at $R > R_e$ in Figs 8 and 10 may be due to a steepening of the [$\alpha$/Fe] profile at large galactocentric distances, as observed by CGA10, or, alternatively, it can be a true change in [Z/H], implying that the result of CGA10 does not apply to the entire population of ETGs in our sample (Arnold et al. 2011; Forbes et al. 2011). The fact that we obtain similar trends of *Age* and [Z/H] for both $\tau$ and SSP models favours a true variation of the metallicity profile in the galaxy outskirts rather than a variation of the star formation time-scale (i.e. abundance ratios) at large radii. In this regard, our results are more consistent with those recently presented by Greene et al. (2012), who found, for a sample of eight massive ETGs, that metallicity gradients seen within the effective radius continue to fall to outer radii of $\sim$2.5 $R_e$, while in contrast, [$\alpha$/Fe] does not drop substantially at large radii in these objects. Notice that so far no significant abundance ratio gradients have been detected in ETGs (e.g. Kuntschner et al. 2010; Spolaor et al. 2010).

## 7 THE EFFECT OF GALAXY ENVIRONMENT

Fig. 12 compares the radial profiles of age and metallicity for the subsamples of field and group ETGs (Section 2). For each subsample, we derive the median $\langle g - X \rangle$ colour profiles ($X = rizYHK$) and fit them, at the fiducial galactocentric distances, as described in Section 5.2. We show here only the results of fitting CB07SC SSPs, for comparison with our previous work (e.g. LF11), and those obtained for one of the CB* models (CB*MC), as other models arrive at similar conclusions (see Section 6.1). Solid and dashed curves in the figure refer to field and group galaxies, respectively. Black symbols and error bars, on the left- and right-hand sides of each panel, represent the mean values of age and metallicity along with their error bars at the extreme fiducial points of 0.1 and 8$R_e$, respectively. The mean values are obtained by averaging the values of age and metallicity for the three mass bins at the extreme fiducial points of 0.1 and 8 $R_e$, respectively. For each subsample, we derive the inner and outer age (metallicity) gradients, $\nabla_{t,i}$ and $\Delta_t$ ($\nabla_{Z,i}$ and $\nabla_{Z,o}$), as described in Section 6. Their values are reported in Tables 9 and 10, for CB07SC and CB*MC models, respectively.

*Central ages.* In the inner region ($R \leq R_e$), group ETGs have positive age gradients (age increasing outwards) for each mass bin ($\nabla_{t,i} > 0$), with the strongest gradients at high mass. On the other hand, field ETGs exhibit flatter $\nabla_{t,i}$. For CB07SC SSPs, field galaxies vary from (slightly negative but consistent with) zero gradients at low mass ($\nabla_{t,i} = -0.01 \pm 0.06$) to slightly positive at high mass ($\nabla_{t,i} \sim 0.05$), while for CB*MC, the $\nabla_{t,i}$ is positive, but consistent with zero (at the $\sim 1\sigma$ level; see Table 10) for all mass bins. These findings are consistent with our previous results (LF11), based on a larger sample of SPIDER ETGs, where field ETGs (at low and intermediate mass) are found with negative – but small – age gradients (consistent with e.g. Ferreras et al. 2009a).

*Central metallicities.* No significant difference is detected, within the errors, between the $\nabla_{Z,i}$ of field and group ETGs, although for CB*MC models, at high mass, the metallicity gradient is significantly steeper for group ($\nabla_{Z,i} \sim -0.58$) relative to field ($\nabla_{Z,i} \sim -0.37$) ETGs. Note that LF11, based on larger samples of ETGs (i.e. smaller error bars on $\nabla_{Z,i}$), found the inner metallicity gradient of group ETGs to be steeper (at all masses), by about $-0.05$, than that of field galaxies. On average, at 0.1 $R_e$, group ETGs are more metal rich than their field counterparts, with $\delta(\log Z/Z_\odot) = 0.05 \pm 0.02$ (CB07SC) and $\delta(\log Z/Z_\odot) = 0.08 \pm 0.03$ (CB*MC), averaging over all three mass bins (see star symbols in the left-hand side of each bottom panel in Fig. 12).

*Outer ages.* In the galaxy outskirts ($R > R_e$), for group ETGs, the *Age* keeps increasing outwards, with very old ages at the furthest radial distances probed. Averaging over all three mass bins, for group ETGs, we find $\langle \Delta_t \rangle = 0.25 \pm 0.05$ dex (CB07SC) and $\langle \Delta_t \rangle = 0.43 \pm 0.09$ dex (CB*MC). In contrast, for field ETGs, the *Age* trend is strongly dependent on the SP model one adopts to fit the colour profiles. For CB07SC, *Age* does not increase significantly with galactocentric distance, with $\langle \Delta_t \rangle = 0.01 \pm 0.07$ dex, while for CB*MC, *Age* increases outwards, with $\langle \Delta_t \rangle = 0.21 \pm 0.08$ dex. Hence, field ETGs have either positive or null age gradients in the outskirts (depending on the model), while group ETGs have positive age gradients in the outskirts.

*Outer metallicities.* For group ETGs, the metallicity gradient is found to steepen in the galaxy outskirts when using CB07SC models ($\langle \nabla_{Z,o} \rangle = -0.8 \pm 0.1$, compared to $\langle \nabla_{Z,i} \rangle = -0.38 \pm 0.02$, averaging all three mass bins). This result is somewhat model dependent, being confirmed – for CB* models – only at low and intermediate mass ($\langle \nabla_{Z,o} \rangle = -0.57 \pm 0.07$ compared to $\langle \nabla_{Z,i} \rangle = -0.36 \pm 0.03$). For field ETGs, no steepening is observed at intermediate and high mass, for both CB07SC and CB*MC models. At low mass, galaxies in the field also exhibit a steeper gradient in the outskirts, for all models ($\nabla_{Z,o} \sim -0.87$ with respect to $\nabla_{Z,i} \sim -0.32$, for CB07SC, and $\nabla_{Z,i} \sim -0.37$, for CB*MC). Hence, the steepening of the metallicity gradients in low-mass ($M_\star \sim 4 \times 10^{10}\,M_\odot$) ETGs is

Downloaded from https://academic.oup.com/mnras/article/426/3/2300/988992 by guest on 06 June 2022

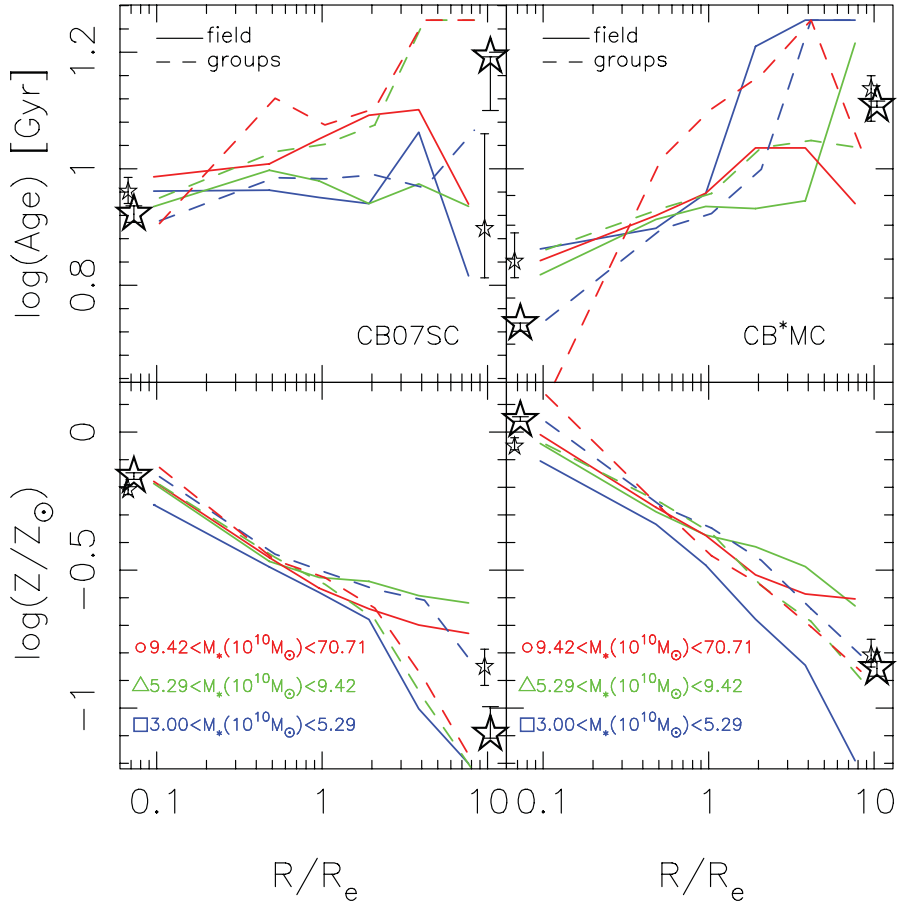



**Figure 12.** Comparison of age (upper panels) and metallicity (lower panels) profiles of field (solid curves) and group (dashed curves) ETGs. Left- and right-hand panels refer to CB07SC and CB*MC models, respectively (see labels in the lower-right of top panels). For $R = 0.1R_e$ ($R = 8R_e$), the mean values of age and metallicity are plotted with black star symbols on the left (right) side of each panel, with small and big stars corresponding to field and group galaxies, respectively. Black error bars are the mean errors on age and metallicity at $R = 0.1R_e$ and $R = 8R_e$.

**Table 9.** Metallicity ($\nabla_Z$) and age ($\nabla_t$) gradients of ETGs as a function of environment, for CB07SC SSP models. The subscripts *i* and *o* refer to the inner ($R \leq R_e$) and outer ($R_e < R < 8R_e$) radial ranges where gradients are estimated.

| Mass range | $\nabla_{Z,i}$ | $\nabla_{Z,o}$ | $\nabla_{t,i}$ | $\Delta_t$ |
|---|---|---|---|---|
| | | Field ETGs | | |
| $3.00 < M_\star[10^{10}\,M_\odot] < 5.29$ | $-0.32 \pm 0.04$ | $-0.87 \pm 0.25$ | $-0.01 \pm 0.06$ | $-0.02 \pm 0.11$ |
| $5.29 < M_\star[10^{10}\,M_\odot] < 9.42$ | $-0.35 \pm 0.04$ | $-0.13 \pm 0.17$ | $0.05 \pm 0.05$ | $0.01 \pm 0.11$ |
| $9.42 < M_\star[10^{10}\,M_\odot] < 70.71$ | $-0.39 \pm 0.03$ | $-0.15 \pm 0.22$ | $0.06 \pm 0.05$ | $0.06 \pm 0.10$ |
| | | Group ETGs | | |
| $3.00 < M_\star[10^{10}\,M_\odot] < 5.29$ | $-0.36 \pm 0.04$ | $-0.47 \pm 0.18$ | $0.08 \pm 0.05$ | $0.10 \pm 0.08$ |
| $5.29 < M_\star[10^{10}\,M_\odot] < 9.42$ | $-0.36 \pm 0.03$ | $-0.92 \pm 0.12$ | $0.10 \pm 0.04$ | $0.25 \pm 0.04$ |
| $9.42 < M_\star[10^{10}\,M_\odot] < 70.71$ | $-0.41 \pm 0.03$ | $-0.94 \pm 0.25$ | $0.20 \pm 0.04$ | $0.30 \pm 0.10$ |

detected in all environments, independent of the SP model one adopts to fit the colour profiles (consistent with that found in Section 6.1). Notice that at $8R_e$, group ETGs are on average less metal rich than their field counterparts,[4] in contrast to the observations in the inner region (see above).

[4] This is truly the case only for high- and intermediate-mass ETGs. In fact, as one can see in the bottom panels of Fig. 12, the green and red dashed lines fall systematically below the green and red solid lines at $R/R_e > 2$. At low mass, group ETGs are more metal rich than their field counterparts, at all masses.

## 8 SUMMARY AND CONCLUSIONS

We have used optical (SDSS-DR6) and near-infrared (UKIDSS-DR4) data for 674 massive ETGs to measure, for the first time, colour gradients out to $\sim 8R_e$, and study how ETGs assemble their mass. The sample comprises systems found in galaxy groups and in the field, with stellar masses ranging from $\sim 3 \times 10^{10}\,M_\odot$ to $\sim 7 \times 10^{11}\,M_\odot$. The critical systematic effects that may affect our conclusions have been carefully taken into account, and we show that none of them (e.g. sky subtraction, colour dependence of the PSF outer wings and the approach adopted to derive the colour

© 2012 The Authors, MNRAS **426,** 2300–2317
Monthly Notices of the Royal Astronomical Society © 2012 RAS

Downloaded from https://academic.oup.com/mnras/article/426/3/2300/988992 by guest on 06 June 2022

**Table 10.** The same as Table 9 but for CB*MC rather than CB07SC SSP models.

| Mass range | $\nabla_{Z,i}$ | $\nabla_{Z,o}$ | $\nabla_{t,i}$ | $\Delta_t$ |
|---|---|---|---|---|
| | | Field ETGs | | |
| $3.00 < M_\star[10^{10}\,M_\odot] < 5.29$ | $-0.37 \pm 0.06$ | $-0.87 \pm 0.30$ | $0.09 \pm 0.08$ | $0.38 \pm 0.09$ |
| $5.29 < M_\star[10^{10}\,M_\odot] < 9.42$ | $-0.34 \pm 0.08$ | $-0.36 \pm 0.16$ | $0.12 \pm 0.13$ | $0.21 \pm 0.13$ |
| $9.42 < M_\star[10^{10}\,M_\odot] < 70.71$ | $-0.37 \pm 0.07$ | $-0.15 \pm 0.16$ | $0.11 \pm 0.08$ | $0.16 \pm 0.06$ |
| | | Group ETGs | | |
| $3.00 < M_\star[10^{10}\,M_\odot] < 5.29$ | $-0.39 \pm 0.06$ | $-0.57 \pm 0.11$ | $0.22 \pm 0.10$ | $0.43 \pm 0.10$ |
| $5.29 < M_\star[10^{10}\,M_\odot] < 9.42$ | $-0.32 \pm 0.03$ | $-0.56 \pm 0.10$ | $0.11 \pm 0.03$ | $0.19 \pm 0.03$ |
| $9.42 < M_\star[10^{10}\,M_\odot] < 70.71$ | $-0.58 \pm 0.04$ | $-0.52 \pm 0.13$ | $0.52 \pm 0.06$ | $0.54 \pm 0.06$ |

profiles) introduces any systematic biases. The stacked colour profiles show remarkable linearity out to $R \sim 8R_e$, getting bluer in the outer regions, irrespective of the mass bin, with the exception of $g - r$ where a curvature is apparent. Nevertheless, this effect is small and does not affect the SP analysis, as the deviations are comparable to the random errors at the radii where the curvature is detected. For the most massive galaxies, the stacked $g - r$ colour profile is compared with that recently obtained by TvD11, finding good agreement.

Colour profiles are translated into SSP-equivalent *Age* and metallicity gradients using a variety of SP models, assuming either a Chabrier or Salpeter IMF, as detailed in Section 5.2. In particular, we exploit the new, state-of-the-art, SP models of Charlot & Bruzual (in preparation), based on different stellar libraries (IndoUS, Miles, STELIB, BaSeL). Errors on both age and metallicity are carefully estimated by accounting for uncertainties on observed colours. We find very unambiguously that metallicity decreases from 0.1 out to $8R_e$ (negative gradient), regardless of the mass bin considered (see Table 5). This result is independent of the adopted SP model and IMF. In addition, we find that the metallicity gradient tends to steepen at large galactocentric radii. The significance of this result changes with the adopted SP models and galaxy mass bin (being more significant at low mass). As for the *Age* parameter, the situation is more complex. From 0.1 to $1\,R_e$, we find that for intermediate- and high-mass ETGs, *Age* increases with radius, while at low mass, no clear trend with galactocentric distance is detected, consistent with our previous results (see e.g. LF11 and references therein). The new result of the present work is that in the outer regions, from 1 to $8R_e$, the SPs of ETGs are even older than in their centres. This is more significant for galaxies in the highest stellar mass bin (i.e. $M_\star \gtrsim 10^{11}\,M_\odot$). We emphasize that using models with extended star formation histories, like exponentially declining ($\tau$) and finite burst models, instead of SSPs, yields similar results within the quoted error bars. We also confirm that the presence of uniformly distributed internal reddening (dust) does not affect the trends of age and metallicity with galactocentric distance.

Finally, we analyse how the age and metallicity profiles depend on the environment where galaxies reside. Group ETGs have positive age gradients out to $\sim 8R_e$, with a very old SP in the outskirts. Their metallicity gradients steepen at $R > 1$–$2\,R_e$. In contrast, field ETGs do not have significant age gradients in the inner region, while at $R \gtrsim 1\,R_e$, the *Age* shows either a flat trend or increases outwards (depending on the model). The metallicity gradient of field ETGs is found to steepen significantly in the outskirts only for low-mass systems. Notice that the results for group galaxies are essentially the same as those for the whole sample of ETGs (see above), consistent with the fact that most of our sample ($\sim$80 per cent) comprises ETGs either residing in (or close to) galaxy groups (see Section 2). Our findings point to the importance of aperture effects when comparing the SP content of ETGs in different environments, as in the galaxy outskirts, group galaxies are older (or coeval, depending on the model) and less metal-rich than field ETGs, while the opposite holds in the central regions, where group ETGs are found to be more metal rich than their field counterparts. This might explain, at least in part, why different results have been reported in the literature about the environmental dependence of the metal content of ETGs (see Paper III), with different studies reporting field ETGs to be more metal rich (Kuntschner et al. 2002; Thomas et al. 2005; de La Rosa et al. 2007; Clemens et al. 2009; Zhu, Blanton & Moustakas 2010), as metal rich as (Bernardi et al. 2006; Annibali et al. 2007) or even more metal poor than their cluster counterparts (Gallazzi et al. 2006).

We have shown here that the SPs in the haloes of ETGs are consistently older and more metal poor than in their cores. This trend depends on mass and, to a lower degree, environment, but overall, the age and metallicity radial gradients are similar for all ETGs in the sample (i.e. more massive than $3 \times 10^{10}\,M_\odot$). Within the core of the galaxies, the observed metallicity gradients – between $\nabla_{Z,i} = -0.3$ and $-0.4$ – are consistent with the simulations of Kobayashi (2004) for non-major merger systems. For galaxies where major-merging is significant, her simulations give shallower metallicity gradients, around $-0.2$. It is worth noting that our metallicity gradients get slightly steeper with increasing mass, supporting the scenario of fast and early formation for the most massive ETGs. Extending the analysis radially out to $8R_e$ allows us to explore the different channels of star formation and assembly in ETGs. Our results are consistent with the scenario of Oser et al. (2010), where two phases of formation operate: an early-phase of in situ star formation – building the core of the galaxy – followed by the accretion of small satellites. The recent simulations of Lackner et al. (2012) quantify in more detail the build up of the stellar component, concluding that major mergers do not dominate the accretion history of massive galaxies, with smaller systems consisting of older, and more metal-poor SPs building up the outer halo, consistent with our analysis. Their simulations suggest age (metallicity) differences of $\Delta t \sim 2.5$ Gyr ($\Delta \log Z \sim -0.15$ dex) between accreted stars and those formed in situ. This process is fully consistent with the observed evolution of massive ETGs on the mass–size plane (see e.g. Daddi et al. 2005; Trujillo et al. 2006; Trujillo, Ferreras & de La Rosa 2011; van Dokkum et al. 2008), where the core is quickly formed during an early phase (see e.g. Ferreras et al. 2009b), followed by the growth of the halo via minor mergers (see e.g. Naab, Johansson & Ostriker 2009).

Downloaded from https://academic.oup.com/mnras/article/426/3/2300/988992 by guest on 06 June 2022

## ACKNOWLEDGMENTS

We thank the anonymous referee for the helpful comments and suggestions that helped us to improve the present manuscript. We have used data from the SDSS (http://www.sdss.org/collaboration/credits.html). GB acknowledges support from the National Autonomous University of México through grants IA102311 and IB102212. We have used data from the 4th data release of the UKIDSS survey (Lawrence et al. 2007), which is described in detail in Warren et al. (2007). Funding for the SDSS and SDSS-II has been provided by the Alfred P. Sloan Foundation, the Participating Institutions, the National Science Foundation, the U.S. Department of Energy, the National Aeronautics and Space Administration, the Japanese Monbukagakusho, the Max Planck Society and the Higher Education Funding Council for England.

## REFERENCES

Adelman-McCarthy J. K. et al., 2008, ApJS, 175, 297
Annibali F., Bressan A., Rampazzo R., Zeilinger W. W., Danese L., 2007, A&A, 463, 455
Aringer B., Girardi L., Nowotny W., Marigo P., Lederer M. T., 2009, A&A, 503, 913
Arnold J. A., Ramanowsky A. J., Brodie J. P., Chomiuk L., Spitler L. R., Strader J., Benson A. J., Forbes D. A., 2011, ApJ, 736, 26
Beers T. C., Flynn K., Gebhardt K., 1990, AJ, 100, 32
Bergval N., Zaricksson E., Caldwell B., 2010, MNRAS, 405, 2697
Berlind A. A. et al., 2006, ApJS, 167, 1
Bernardi M., Nichol R. C., Sheth R. K., Miller C. J., Brinkmann J., 2006, AJ, 131, 1288 (B06)
Bertelli G., Girardi L., Marigo P., Nasi E., 2008, A&A, 484, 815
Bruzual G., 2007, in Vazdekis A., Peletier R., eds, IAU Symp. 241. Stellar Populations as Building Blocks of Galaxies. Cambridge Univ. Press, Cambridge, p. 125
Bruzual G., Charlot S., 2003, MNRAS, 344, 1000 (BC03)
Caon N., Capaccioli M., D'Onofrio M., 1993, MNRAS, 265, 1013
Cappellari M. et al., 2006, MNRAS, 366, 1126
Cappellari M. et al., 2012, Nat, 484, 485
Cardelli J. A., Clayton G. C., Mathis J. S., 1989, ApJ, 345, 245
Carlberg R. G., 1984, ApJ, 286, 403
Carollo C. M., Danziger I. J., Buson L., 1993, MNRAS, 265, 553
Charlot S., Bruzual G., 2007, Unpublished Models Distributed on Demand (CB07)
Cid Fernandes R., González Delgado R. M., Storchi-Bergmann T., Martins L. P., Schmitt H., 2005, MNRAS, 356, 270
Clemens M. S. et al., 2009, MNRAS, 392, 35
Coccato L., Gerhard O., Arnaboldi M., 2010, MNRAS, 407, L26 (CGA10)
Daddi E. et al., 2005, ApJ, 626, 680
Davies R. L., Burstein D., Dressler A., Faber S. M., Lynden Bell D., Terlevich R. J., Wegner G., 1987, ApJS, 64, 581
Davies R. L., Sadler E. M., Peletier R. F., 1993, MNRAS, 262, 650
de Jong R. S., 2008, MNRAS, 388, 1521
de La Rosa I. G., de Carvalho R. R., Vazdekis A., Barbuy B., 2007, AJ, 133, 330
De Vaucoulerus G., 1961, ApJS, 5, 233
Duc P.-A., Renaud F., 2011, Review to be published in Tidal Effects in Astronomy and Astrophysics, Lecture Notes in Physics (arXiv:1112.1922)
Eggen O. J., Lynden Bell D., Sandage A. R., 1962, ApJ, 136, 748
Ferreras I., Lisker T., Carollo C. M., Lilly S. J., Mobasher B., 2005, ApJ, 635, 243
Ferreras I., Lisker T., Pasquali A., Kaviraj S., 2009a, MNRAS, 395, 554
Ferreras I. et al., 2009b, ApJ, 706, 158
Forbes D. A., Spitler L. R., Strader J., Romanowsky A. J., Brodie J. P., Foster C., 2011, MNRAS, 413, 2943
Gallazzi A., Charlot S., Brinchmann J., White S. D. M., 2006, MNRAS, 370, 1106
Gargiulo A., Saracco P., Longhetti M., 2011, MNRAS, 412, 1804
Girardi, Léo et al., 2010, ApJ, 724, 1030
González J. J., 1993, PhD thesis, Univ. California
González-Pérez V., Castander F. J., Kauffmann G., 2011, MNRAS, 411, 1151
Gorgas J., Efstathiou G., Aragón-Salamanca A., 1990, MNRAS, 245, 217
Goudfrooij P., de Jong T., 1995, A&AS, 298, 784
Greene J. E., Murphy J. D., Comerford J. M., Gebhardt K., Adams J. J., 2012, ApJ, 750, 32
Guo Y. et al., 2011, ApJ, 735, 18
Hinkley S., Im M., 2001, ApJ, 560, L41
Hyde J. B., Bernardi M., 2009, MNRAS, 394, 1978
Ilbert O. et al., 2006, A&A, 457, 841
Kereš D., Katz N., Weinberg D. H., Davé R., 2005, MNRAS, 363, 2
Kobayashi C., 2004, MNRAS, 347, 740
Komatsu E. et al., 2011, ApJS, 192, 18
Kormendy J., Fisher D. B., Cornell M. E., Bender R., 2009, ApJS, 182, 216
Kriek M. et al., 2010, ApJ, 722, L64
Kuntschner H., Smith R. J., Colless M., Davies R. L., Kaldare R., Vazdekis A., 2002, MNRAS, 337, 172
Kuntschner H. et al., 2010, MNRAS, 408, 97
La Barbera F., de Carvalho R. R., 2009, ApJ, 699, L76
La Barbera F. et al., 2008, PASP, 120, 681
La Barbera F., de Carvalho R. R., de la Rosa I. G., Lopes P. A. A., Kohl-Moreira J. L., Capelato H. V., 2010a, MNRAS, 408, 1313 (Paper I)
La Barbera F., Lopes P. A. A., de Carvalho R. R., de La Rosa I. G., Berlind A. A., 2010b, MNRAS, 408, 1361 (Paper III)
La Barbera F., de Carvalho R. R., de La Rosa I. G., Gal R. R., Swindle R., Lopes P. A. A., 2010c, AJ, 140, 1528 (Paper IV)
La Barbera F., Ferreras I., de Carvalho R. R., Lopes P. A. A., Pasquali A., de la Rosa I. G., de Lucia G., 2011, ApJ, 740, 41 (LF11)
Lackner C. N., Cen R., Ostriker J. P., Joung M. R., 2012, MNRAS, 425, 641
Lançon A., Mouhcine M., 2002, A&A, 393, 167
Larson R. B., 1974, MNRAS, 166, 585
Larson R. B., 1975, MNRAS, 173, 671
Lawrence A. et al., 2007, MNRAS, 379, 1599
Le Borgne J.-F. et al., 2003, A&A, 402, 433
Lopes P. A. A., de Carvalho R. R., Kohl-Moreira J. L., Jones C., 2009, MNRAS, 392, 135
McClure R. D., 1969, AJ, 74, 50
Marigo P., Girardi L., 2007, A&A, 469, 239
Marigo P., Griardi L., Bressan A., Groenewgen M. A. T., Silva L., Granato G. L., 2008, A&A, 482, 883
Mehlert D., Thomas D., Saglia R. P., Bender R., Wegner G., 2003, A&A, 407, 423
Melbourne J. et al., 2012, ApJ, 748, 47
Michard R., 2005, A&A, 441, 451
Naab T., Johansson P. H., Ostriker J. P., 2009, ApJ, 699, L178
Oser L., Ostriker J. P., Naab T., Johansson P. H., Burkert A., 2010, ApJ, 725, 2312
Pasquali A., Gallazzi A., Fontanot F., van den Bosch F. C., De Lucia G., Mo H. J., Yang X., 2010, MNRAS, 407, 937
Peletier R. F., Valentijn E. A., Jameson R. F., 1990, A&A, 233, 62
Pipino A., DÉrcole A., Matteucci F., 2008, A&A, 484, 679
Pipino A., DÉrcole A., Chiappini C., Matteucci F., 2010, MNRAS, 407, 1347
Rayner, Cushing M. C., VAcca W. D., 2009, ApJS, 185, 289
Roche N., Bernardi M., Hyde J., 2010, MNRAS, 407, 1231
Roediger J. C., Courteau S., MacArthur L. A., McDonald M., 2011, MNRAS, 416, 1996
Saglia R. P., Maraston C., Greggio L., Bender R., Ziegler B., 2000, A&A, 360, 911
Salpeter E. E., 1955, ApJ, 121, 161

Downloaded from https://academic.oup.com/mnras/article/426/3/2300/988992 by guest on 06 June 2022

Sánchez-Blázquez P. et al., 2006a, MNRAS, 371, 703
Sánchez-Blázquez P., Gorgas J., Cardiel N., 2006b, A& A, 457, 823
Savoy J., Welch G. A., Fich M., 2009, ApJ, 706, 21
Silva D. R., Elston R., 1994, ApJ, 428, 511
Silva D. R., Wise M. W., 1996, ApJ, 457, 15
Spolaor M., Kobayashi C., Forbes D. A., Couch W. J., Hau G. K. T., 2010, MNRAS, 408, 272
Suh H., Jeong H., Oh K., Yi S. K., Ferreras I., Schawinski K., 2010, ApJS, 187, 374
Swindle R., Gal R. R., La Barbera F., de Carvalho R. R., 2011, AJ, 142, 118S (Paper V)
Tal T., van Dokkum P. G., 2011, ApJ, 731, 89 (TvD11)
Thomas D., Maraston C., Bender R., Mendes de Oliveira C., 2005, ApJ, 621, 673
Tortora C., Napolitano N. R., Cardone V. F., Capaccioli M., Jetzer P., Molinaro R., 2010, MNRAS, 407, 144
Trujillo I. et al., 2006, ApJ, 650, 18
Trujillo I., Ferreras I., de La Rosa I. G., 2011, MNRAS, 415, 3903
Valdes F., Gupta R., Rose J. A., Singh H. P., Bell D. J., 2004, ApJS, 152, 251
van Dokkum P. G., Conroy C., 2011, ApJ, 735, 13
van Dokkum P. G. et al., 2008, ApJ, 677, L5
Warren S. J. et al., 2007, MNRAS, 375, 213
Westera P., Lejeune T., Buser R., Cuuisinier F., Bruzual G., 2002, A&A, 381, 524
Wise M. W., Silva D. R., 1996, ApJ, 461, 155
Worthey G., 1994, ApJS, 95, 107
Wu H., Shao Z., Mo H. J., Xia X., Deng Z., 2005, ApJ, 622, 244
Zhu G., Blanton M. R., Moustakas J., 2010, ApJ, 722, 491
Zibetti S., Gallazzi A., Charlot S., Pierini D., Pasquali A., 2012, MNRAS, submitted (arXiv:1205.4717)

## APPENDIX A: COMPARISON OF PARAMETRIC AND NON-PARAMETRIC LIGHT PROFILES

Fig. A1 compares parametric and non-parametric stacked light profiles for each of the three galaxy mass bins (from left to right), and each waveband, $X = grizYHK$ (from top to bottom), used in the present study. We do not consider $J$ band, as this is not used for the SP analysis (see Section 4 for details). For each galaxy image, and a given waveband $X$, we measure mean surface brightness values on a set of concentric circles, with radii equally spaced by 0.5 pixels, out to a maximum distance of $\sim$110 arcsec from the galaxy centre. All objects around the given galaxy are masked out with the software 2DPHOT, as described in La Barbera et al. (2008). The surface brightness profiles of all galaxies are scaled by the corresponding $R_{e,X}$, and normalized to have the same flux (within an aperture of $2R_{e,X}$). The so-normalized profiles are averaged within radial bins logarithmically spaced by 0.15 dex. This procedure provides non-parametric light profiles (not corrected for PSF), with grey regions in Fig. A1 marking the $1\sigma$ mean confidence contours around them. The same procedure, applied to the PSF-convolved best-fitting two-dimensional Sérsic models, gives the parametric light profiles, plotted as black curves in Fig. A1. Overall, we find a good agreement between observed and model profiles, out to the largest galactocentric distances considered in this work ($\sim 8R_e$). This supports previous claims that a single Sérsic law is able to describe accurately the light distribution of ETGs out to $\sim 8R_e$ (Kormendy et al. 2009; TvD11), supporting the robustness of our parametric colour estimates over a wide radial range.

Downloaded from https://academic.oup.com/mnras/article/426/3/2300/988992 by guest on 06 June 2022

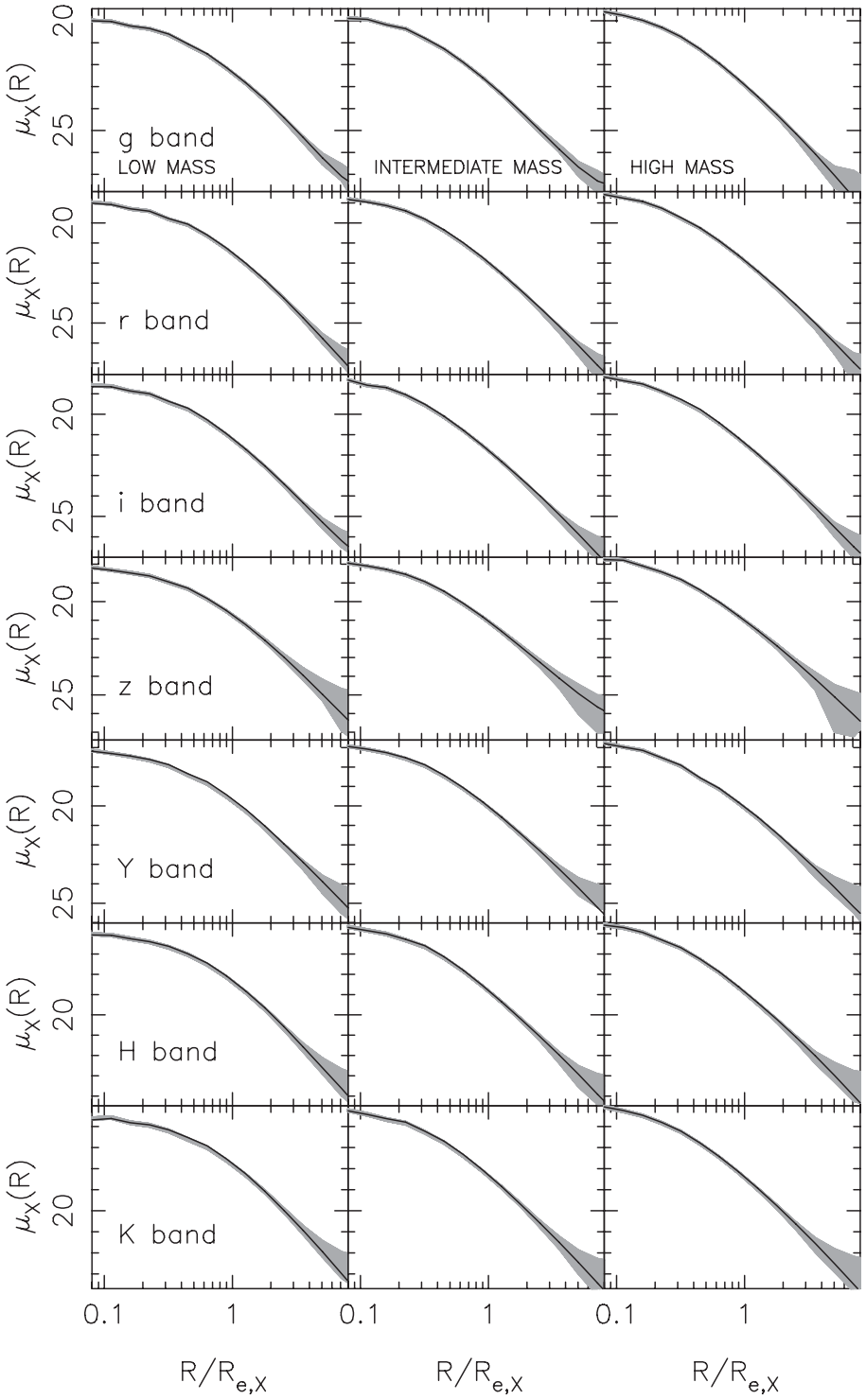



**Figure A1.** Comparison of parametric and non-parametric light profiles for low- (left-), intermediate- (middle), and high-mass (right-hand panels) ETGs, and each waveband out of $X = rizYHK$ (from top to bottom, as labelled in left-hand panels). Black lines are the parametric profiles, while grey regions mark the 1 $\sigma$ mean confidence intervals around non-parametric profiles. Notice that black curves fall in the grey regions for all mass bins, and all wavebands, supporting our approach to estimate colour profiles.

This paper has been typeset from a TEX/LATEX file prepared by the author.

Downloaded from https://academic.oup.com/mnras/article/426/3/2300/988992 by guest on 06 June 2022